PHIBSS FIBS - A SCUBA2 FOLLOWUP OF Z $\sim$ 2.5, GAS RICH, STAR FORMING GALAXIES

by

Jennifer K. Beanlands

A Thesis Submitted to
Saint Mary's University, Halifax, Nova Scotia
in Partial Fulfillment of the Requirements for
the Degree of Master of Science in Astronomy
(Department of Astronomy and Physics)

August 2015, Halifax, Nova Scotia

Approved: Dr. Scott Chapman
Advisor

Approved: Dr. Robert Thacker
Examiner

Approved: Dr. Ian Short
Examiner

Date: August 27, 2015

Acknowledgements

I would first like to thank my supervisor, Dr. Scott Chapman, for his invaluable guidance and assistance throughout this journey. Your understanding has not been lost on me. I would also like to thank my co-supervisor, Dr. Robert Thacker, for agreeing to take me on.

To the group at Dalhousie: thank you for welcoming me into your space.

To Kevin Lacaille and Maan Hani: without your willingness to drop everything and lend a helping hand, I would never have finished. Thank you.

Finally, I would like to thank my family, who have supported me every step of way. I am so glad you got to see this happen.

Contents

List of Tables

List of Figures

PHIBSS FIBS - A SCUBA2 FOLLOWUP OF Z $\sim$ 2.5, GAS RICH, STAR FORMING GALAXIES

Jennifer K. Beanlands

August 27, 2015

Abstract

Emissions from high redshift (i.e. $z \sim 2.5$), star forming galaxies provide a unique window into the state the universe at earlier epochs, and how these galaxies evolve over time. Accurate studies of these galaxies, however, require the ability to distinguish between different types of objects. The Institut de Radioastronomie Millimétrique Plateau de Bure High-z Blue Sequence Survey (Tacconi et al. 2010) aims to understand the gas content in massive, star forming galaxies. To date, Hα and ultraviolet emission, along with CO(3-2) emission were used to derive star formation rates, and estimate gas masses respectively. This thesis focuses on the high redshift sample of these galaxies and uses far-infrared emission to learn more about the interstellar medium and star formation rates of these objects. Results show, however, that 23% of these galaxies are not what they seem. Two of the objects appear to be submillimetre galaxies, and two likely host active galactic nuclei.

Chapter 1

Introduction

The peak of the global star formation rate (SFR) of the universe and active galactic nuclei (AGN) activity, coincide at redshifts between $\sim$ 2 - 3. Observing galaxies at this epoch helps uncover what the universe was like during it's busiest time and is key to understanding both galactic evolution, as well as the evolution of the entire universe. Estimating the SFR of particular galaxies during this epoch gives us a better and more precise understanding of this peak, along with what might be driving it. Likewise, determining the dust mass in these galaxies is important because it is a crucial part of understanding the physics of the interstellar medium (ISM) which directly impacts the production of stars. Indeed, studying the evolution of the ISM allows for a more robust understanding of galaxy evolution.

The ideal method of characterizing the ISM and SFR of galaxies is to use a multi-wavelength approach which allows a robust and precise derivation. In many cases, however, multi-wavelength data is not available, or is not feasible given observational time constraints. Single wavelength studies of high redshift, star forming galaxies are a good first estimate of many of the fundamental properties of these objects. For example, Scoville et al (2014) found that long wavelength emission from the dust continuum in the optically thin Rayleigh-Jeans regime could accurately describe the ISM of a wide range of star forming galaxies, both local and those at high redshifts. Genzel et al. (2015) showed similar results when using dust emission to characterize both gas mass, and the total ISM. This

makes single waveband data from submillimetre observations ideal probes of the ISM, through the estimation of total dust mass.

Star formation rates can be also be constrained using both submillimetre, and 24μm emission. Observed frame 24μm wavelength emission is particularly good at estimating SFR in high redshift galaxies because of its direct link to poly-cyclic aromatic hydrocarbon (PAH) emission. Likewise, submillimetre emission is a good indicator of SFR because the cool dust re-radiates higher energy emission from newly formed stars.

Observations at both the submillimetre and far-infrared wavebands can be very important in understanding galaxies as a whole. For example, embedded and obscured AGN may be invisible to an observer not looking specifically for emission from dusty tori. The presence of an AGN, however, has broad implications for understanding and interpreting emission at all wavelengths. Likewise, without observing in the submillimetre waveband, the extreme dusty emission indicative of submillimetre galaxies would be lost, and so the actual morphology and physics of the observed galaxy could be overlooked. We have shown this to be the case in the high redshift galaxy sample of the IRAM Plateau de Bure High-z Blue Sequence Survey (PHIBSS). Out of seventeen objects considered by this survey to be regular, star forming galaxies, we determined two to be submillimetre galaxies and another two to be active galaxies, hosting obscured AGN. This has implications both for the derived gas mass and the inclusion of these objects in a general galactic 'main sequence'.

1.1 IRAM Plateau de Bure High-z Blue Sequence Survey

The IRAM Plateau de Bure High-z Blue Sequence Survey (PHIBSS) is a large CO study of massive, optically and UV selected, star forming galaxies

near the peak of global star formation. The initial results were published by Tacconi et al. (2010) and Tacconi et al. (2013), who used the IRAM Plateau de Bure Millimetre Interferometer (PdBI) to derive the gas masses of these galaxies through CO 3-2 emission. They found that these galaxies did indeed lie on the galactic main-sequence and categorized them as normal, star-forming galaxies.

The entire sample of galaxies in the PHIBSS survey were reported by Tacconi et al. 2013, and reside in two redshift bins. The first bin is at relatively low redshift, and consists of 38 galaxies between redshifts of $z = 1$ and $z = 1.5$. The galaxies in this bin were selected from the All-Wavelength Extended Growth Strip (EGS) International Survey which has extensive imaging from radio to optical wavelengths. The PHIBSS objects were selected from the EGS data with appropriate [OII] spectroscopic redshifts, stellar masses greater than $2.5 \times 10^{10}\,\mathrm{M}_{\odot}$, and SFRs greater than 30 $\mathrm{M}_{\odot}$ yr^{-1}. Further criteria prioritized those objects residing in the CANDELS and 3D-HST fields.

The 14 galaxies in the high redshift bin reside between redshifts of $z = 2$ and $z = 3$, and are the primary target of this work. These galaxies were selected from the $z \sim 2$ UV-colour-magnitude survey by Steidel et al. (2004). From this survey, galaxies with the same properties as the low redshift bin were chosen from an Hα subset reported by Erb et al. (2006). While these properties provide a generally representative sample of star forming galaxies at this redshift, the UV selection criteria of the original Steidel et al. (2004) study does bias the sample away from dusty galaxies.

All of the galaxies in the Tacconi et al. (2013) study were observed at 2 and 3 millimetre wavelengths (depending on redshift) with the PdBI. The luminosity from CO line emission was converted into a gas mass in order to study star forming galaxies over a variety of redshifts. Eight of the low redshift objects, and one in the high redshift bin (BX610) were selected for higher resolution imaging.

1.2 Submillimetre Astronomy

Submillimeter astronomy is a relatively new branch of observational astronomy which deals primarily with radiation between wavelengths of 0.3 and 1mm. This range is particularly important in understanding cold dust and gas in the high redshift universe because the blackbody emission from low temperature dust peaks in this region. Likewise, higher energy emission from young stars is generally re-radiated by dust in the submillimetre range, which makes it an excellent probe of both star formation, and the ISM.

Observations at submillimeter wavelengths have been undertaken by a wide variety of instruments both from the ground and in space. Submillimetre telescopes are comprised of either large, single dishes such as the James Clerk Maxwell Telescope (JCMT), or higher resolution, multi-antennae interferometers like the Atacama Large Millimeter/submillimetre Array (ALMA). Space Based submillimeter telescopes such as the *Hershel Space Observatory* (formerly the *Far Infrared and Submillimetre Telescope*), have also been useful because they remove the problems with electromagnetic radiation absorption due to water vapour in the Earth's atmosphere. Submillimetre astronomy has also been conducted from near-space telescopes, which use airborne telescopes to mitigate atmospheric problems. One of these near-space telescopes is the Stratospheric Observatory for Infrared Astronomy (SOFIA), which incorporates a 2.5 meter telescope attached to a modified Boeing 747SP widebody aircraft. Another is the Balloon-borne Large Aperture Submillimeter Telescope (BLAST), which uses a 2 metre, submillimetre telescope attached to a high altitude monitoring balloon.

Continuum emission at submillimeter wavelengths has been historically difficult to observe and combines methods used by both optical and radio telescopes. The detectors used in submillimeter telescopes generally use bolometer

arrays, which employ materials with temperature-dependent resistance to measure incident radiation and has proven to be extremely effective at these wavelengths. Bolometer arrays usually consist of transition edge sensors (TES) and Superconducting Quantum Interface Device (SQUID) amplifiers. A TES array works by cooling the sensors to their sub-kelvin transition temperatures, where a small change in temperature from an incident photon will create a small, but measurable change in resistance of the sensor. The signal is then boosted by a SQUID amplifier, which is a very sensitive magnetometer that boosts the faint electrical signal to assist in readout.

1.2.1 Atmospheric Transmission

One of the issues with ground based astronomy is the transmission of radiation through the Earth's atmosphere. While it is fortunate for life on earth that the atmosphere blocks out high energy UV and X-ray radiation, astronomers find this a considerable problem. Many wavelengths, even at low energies, are not observable from the ground, hence the need for space based telescopes. Atmospheric transmission at submillimetre wavelengths is poor (primarily due to water vapour) which is what makes submillimeter astronomy so difficult. There are, however, some wavelength windows which allow for better transmission which reside in discrete wavebands at approximately 350μm, 450μm, 770μm, and 870μm. This is also one of the reasons why submillimetre telescopes are placed at high elevations, which limits the amount of atmosphere that the telescope must look through. For example, the JCMT is located at at an elevation of 4098 meters, which raises it above 97% of the water vapour found in the atmosphere. Altitude, however, is not the only method of limiting water vapour in the atmosphere. The South Pole Telescope, for example, is located in Antarctica which is at a relatively low altitude, however the water vapour in the atmosphere is crystallized making it the best submillimetre sight on earth.

1.2.2 Submillimetre Galaxies

In the late 1990s, the Submillimetre Common-User Bolometer Array (SCUBA) on the 15 meter JCMT provided the first deep field pointings at 850um. The maps that were produced showed a large number of bright, high redshifted galaxies that could not be detected at optical wavelengths, with surface densities significantly higher than that of the local universe. The objects detected are now known as submillimetre galaxies (SMGs), and typically have 850μm fluxes of $S_{850} \geq 4$ mJy. Residing between $z = 1$ - 3, SMGs are a subset of what is known as dusty star-forming galaxies, and are undergoing intense star formation with upwards of 1000 $M_{\odot}yr^{-1}$ in some cases (e.g. Barger et al. 2014). Although their proposed local counterparts, Ultraluminous InfraRed Galaxies (ULIRGs), are relatively rare, submillimetre galaxies can have spatial densities $\sim$ 1000 times higher, making them relatively common objects at high redshift. Their relative ubiquity, combined with their intense SFRs, contribute up to half of the star-formation rate density of the universe at redshifts of $\sim$ 2 (e.g. Hughes et al. 1998, Smail et al. 2002, Casey et al. 2013). The emission from higher energy wavelengths tends to be obscured because of the high dust content in SMGs which absorbs and re-radiates much of the optical and UV radiation at lower energy wavelengths.

The morphology of SMGs, along with their local counterpart, ULIRGs, has been highly debated, with research still ongoing. The question is: "What is driving the intense star formation within these galaxies?" The debate seems to concentrate mainly around whether or not these objects are massive, secular disks, or major mergers. Tacconi et al (2008) obtained the gas kinematics for four SMGs, and showed that two of them have multiple morphologies, with the other two appearing to be turbulent disks which are the remnants of a galactic merger. However, computational research from Hayward et al. (2013) shows that up to 50% of blended submillimetre sources are line of sight projections phenomena and

not physically interacting. While this has not yet been demonstrated observationally, it is likely that lower luminosity SMGs are populated by turbulent disks, and the highest luminosity galaxies are major mergers.

The number density of SMGs appears to have evolved over the history of the universe, with the bulk of SMGs residing at high redshift. Chapman et al. (2005) found that the median redshift of radio detected SMGs was $z = 2.2$, which was further supported by Simpson et al (2014) who's ALMA survey of 96 submillimetre galaxies shows a median photometric redshift of $z = 2.5 \pm 0.2$. Furthermore, they determined that, at most, only 35% of the total SMG population resides at $z \geq 3$. Recently, the use of gravitational lensing has been used to boost the signal of high redshift submillietre galaxies, revealing a tail at $z > 4$ (Vieira et al 2013) with the most distant SMG to date residing at $z = 6.34$ (Riechers et al. 2013).

Submillimetre galaxies are not only interesting as high redshift objects, but also because of their evolution. It has been proposed that submillimetre galaxies may be an evolutionary phase of the massive, quiescent ellipticals we see in the universe today. This claim has been reinforced observationally by Simpson et al. (2014) who show that decedents of ALMA detected SMGs at redshifts of zero would have approximately the same spacial density as local quiescent galaxies. They also found that the lookback times of the SMGs in their sample coincides with the mass-weighted ages of the local ellipticals, providing good evidence to support the idea of SMGs as progenitors. Similarly, Hai et al (2013) found that a massive colliding system at $z = 2.3$ will likely become a massive elliptical galaxy with a stellar mass of 4×10^{11} $M_{\odot}$ by $z \sim 1.5$. Swinbank et al. (2006) also found that the six, luminous SMGs in their study would evolve on to the Faber-Jackson relation and would have a similar spatial density to that of local, massive ellipticals. While not yet definitive, there is strong evidence for the

idea of submillimetre galaxies evolving into massive ellipticals, which has serious implications for extragalactic astronomy in general, and gives some insight into how the universe is evolving.

1.2.3 Negative K-correction

One of the most useful properties of SMGs, is that their infrared emission has a nearly constant flux out to high redshifts, due to a negative k-correction. Because the emission from distant galaxies is redshifted, the observed emission must be corrected to rest-frame wavelengths. This correction is known as the k-correction and depends on the shape of the spectral energy density (SED) of the galaxy. The SED of a submillimetre galaxy has a positive slope at infrared wavelengths because of the modified blackbody emission produced by the massive amount of dust. This emission peaks at $\sim$100μm, meaning that the flux density between 850μm and 2mm is located in the Rayleigh-Jeans regime and increases with increasing redshift, hence the negative k-correction. The negative k-correction is so significant that it negates cosmological dimming, where the flux of an object decreases as $1/D_L^2$. This means that the flux of a galaxy around 850μm will remain constant from $z \sim 1-8$, providing an extremely useful property for investigating the early universe.

This negative K-correction makes SMGs unique in the universe because we can observe galaxies at high redshift as easily as ones we can in the relatively local universe. This property alone provides some insight into the evolution of cosmic star formation rate density (CSFRD). If the occurrence of SMGs (and subsequently, the cosmic star formation rate) is independent of redshift, we should expect to see equal numbers of SMGs in the local universe and at higher redshifts. However, as previously stated, ULIRGs are extremely rare in the universe whereas

SMGs are comparatively more common at high redshift. With a CSFRD contribution from SMGs of up to 50% at z $\sim$ 2 (Casey, Narayanan & Cooray, 2014), this reinforces the already well established idea that the CSFRD is changing with redshift.

1.2.4 Beam Size, Multiplicity and Selection bias

One of the historical problems with submillimetre astronomy is the large beam size of single dish telescopes employed in this field. At 850μm, for instance, the SCUBA-2 instrument on JCMT has a beam size of 15 arcseconds, which means that it can be nearly impossible to find the position of an observed object, or even to determine if its emission has multiple counterparts. This means that a single galaxy observation is nearly impossible unless a multi-wavelength approach is used. For example, at least 35% (and up to 50%) of submillimetre sources detected with the Large APEX Bolometer Camera (LABOCA) on the Atacama Pathfinder Experiment (APEX) telescope break down into multiple galaxies when observed with higher resolution telescopes (Hodge et al. 2013)

Fortunately, there exists a far-infrared/radio correlation in local starburst galaxies (Ivison et al., 1998) which also exists for higher redshift galaxies. The smaller beam size on radio telescopes allow a large area of submillimetre emission to be broken down into its individual radio detected counterparts. Unfortunately, these radio-selected SMGs bias the sample, because radio-quiet galaxies will not be included (Chapman et al. 2003). This is highlighted by Hodge et al. (2013) who found that 45% of submillimetre galaxies had no radio counterparts and were therefore overlooked. Furthermore, there is no negative k-correction at radio wavelengths, so high redshift objects are undetected.

The issue of radio selection bias has led to further attempts at multi-wavelength SMG identification, specifically at 24μm. There are, unfortunately,

issues at this wavelength as well. Emissions at 24μm are produced by warm dust, rather than the cold dust detected in the far-infrared, and only a loose correlation exists between the two. This is because there are two possible methods of heating for warm dust: dense star-forming regions and dusty tori (Figure 1.1) surrounding central supermassive black holes. Furthermore, at intermediate redshifts, the 24μm spectrum is dominated by PAHs (Lagache et al. 2004) and silicates, leading to irregular detection frequency, and further biasing. However, the high resolution of 24μm telescopes and the fact that the density of 24μm sources is much higher than that of radio sources, makes it a useful tool in helping to break up a submillimetre detection into its individual components, allowing for a relatively easy method of dealing with multiplicity issues. The *Spitzer Space Telescope* has conducted large scale mapping at this wavelength and much of this data is readily available, making it a feasible alternative to radio detection.

New large scale arrays like ALMA are providing unprecedented angular resolution, allowing for the precise identification of individual SMGs, based on submillimetre emission alone. Interferometers like ALMA, the PdBI, and the Caltech Millimeter Array provide an order of magnitude more sensitivity over single dish experiments, allowing for the first unbiased surveys of SMGs. However, what arrays make up for in angular resolution, they lack in field of view, and so large scale surveys are nearly impossible with these telescopes. This makes single dish telescopes like the JCMT integral for the initial large scale surveys, in addition to the multitude of lower priority projects and those that do not require such high resolution.

1.2.5 Dust

Understanding the dust content in galaxies is extremely important to both our understanding of galaxy evolution and our ability to observe galaxies. Unlike

dust on earth, interstellar dust is composed of tiny grains of dielectric and refractory materials and can range in size from a few molecules, to ∼0.1nm in size. Primarily consisting of carbonates, silicates, carbonaceous materials and silicon carbide, dust is usually formed in the atmospheres of red giants, and is deposited into the interstellar medium through supernovae and the winds from asymptotic giant branch stars. Large clouds of dust tend to form through gravitational attraction and

While not a direct contributor to star formation, intergalactic dust plays a significant role in moderating SFR and metallicity. Dust is important in shaping the stellar initial mass function (IMF) because it is very effective both at lowering the ionization temperature of the gas, as well as physically cooling gas clouds (Dopcke et al. 2011) which is a crucial step in star formation as warm gas will not fragment and collapse into stars. Dust also regulates the masses of new stars, allowing less massive stars to be formed in low metallicity environments as well as moderating the formation of short lived, high mass stars. Dust also hinders our ability to observe galaxies, as it blocks out almost all radiation, while concurrently emitting strong infrared radiation. This means that the only way we can observe and understand SMGs is through the indirect, millimetre/submillimetre frame emission, re-radiated by the dust content.

One of the most obvious and important features of submillimetre galaxies is their massive dust content. SMGs can have dust masses upwards of $M \geq 1 \times 10^9$ $M_\odot$ and large gas reservoirs of 10^{10} $M_\odot$ (Greve et al. 2005). Santini et al. (2010) compared high redshift SMGs to local galaxies and found that SMGs tend to have dust-to-stellar mass ratios six times larger than ULIRGs and thirty times larger than local spirals.

SMGs are significantly more dusty than local star forming galaxies, but the origin of this dust is still somewhat of a mystery. Known as the 'dust-budget crisis', dust production by low and intermediate mass stars falls short of the observed dust mass in SMGs by a factor of 240. Even with the addition of supernovae, only 19% of observed galaxies' dust masses can be successfully predicted (Rowlands et al. 2014). While not yet fully understood, models including minimal dust destruction or a top-heavy IMF seem to produce the amount of dust observed in these galaxies.

1.2.6 The Star Formation Main Sequence

The star formation main sequence (SFMS) is an approximately linear relation between SFR and total stellar mass. It has been seen to work over many ranges of redshift, and various wavebands from radio to optical. The idea is that the majority of star forming galaxies are going through a similar, steady processes of star formation, creating a tight correlation between stellar mass and SFR.

While this 'cookie cutter' approach to predicting star formation in galaxies works in many cases, it fails when you include submillimetre galaxies. SMGs have some of the highest SFRs in the universe, but their comparatively normal stellar masses means they they lie well above the SFMS curve. This is important because, while the bulk of galaxies lie on the SFMS, the ones that don't are forming stars so rapidly that they make up a large portion of the global star formation rate density.

1.3 Active Galactic Nuclei

Active Galactic Nuclei are large, rapidly accreting supermassive black holes embedded in the centre of some galaxies. Although most, if not all galaxies contain a supermassive black hole (one defined by a mass upwards of $10^5 M_\odot$)

in their interiors, AGN are unique in that they are surrounded by an extremely energetic and superheated accretion disc comprised of gas and dust which acts as the central engine. These objects are some of the brightest and most energetic in the universe, and while the central engine is on a sub-parsec scale, it can produce radio jets that can be many times larger than that of the host galaxy. Along with jets, AGN can be characterized by their extremely bright central core, non thermal emission, the presence of both broadened and high-excitation emission lines and variability. The energy comes from the gravitational potential energy of the black hole, which drives friction in the accretion disk and energizes the surrounding area.

Observationally, AGN come in a number of flavours exhibiting a wide range of both continuum and emission line phenomena. Arguably the most well known are Seyfert Galaxies which are divided into two categories, Seyfert I and Seyfert II. Seyfert I galaxies are characterized by a strong optical continuum and both narrow and broad emission lines. Seyfert II galaxies produce narrow spectral lines, however they lack the broad lines and strong continuum indicative of Seyfert I's. Quasars, or quasi stellar objects (QSO), are also AGN, however they are differentiated from Seyfert galaxies through their luminosity, where QSOs are on the higher end of the luminosity spectrum. There are also radio loud and radio quiet AGNs, which are a further subset of Seyfert galaxies. The distinction between these two is the intense radio emission coming from the radio loud objects.

These luminous objects pose an interesting question to galaxy evolution: "Are active galaxies unique objects, or does every galaxy have the potential to have an AGN phase at some point in their evolution?" Although not yet fully understood, it is now thought that most galaxies have likely gone through at least one active period during their lifetime, meaning that every galaxy has the potential to be 'turned on'. The AGN phase of galaxy evolution is very important

in that the massive amounts of energy released affects everything from star formation to galaxy cluster dynamics. What may trigger an AGN has been highly debated, and currently there is no clear consensus. The most effective way of triggering an AGN is thought to be through major mergers of two or more galaxies. This process is very effective because the ordered, angular momentum of the system is disturbed, and so large amounts of matter is funnelled into the centre of the galaxy. However, while major mergers are one way of triggering an AGN, it is not the whole picture. One consideration is that not all galaxies have gone though a major merger, but more importantly, while major mergers can explain the brightest of active galaxies, they do not necessarily explain the lower luminosity AGN (Ellison, Patton & Hickox, 2015). While it is thought that AGN may also be triggered by galaxy dynamics (e.g. bars), flybys, and minor mergers, the question of what activates an active galaxy, especially at lower luminosities, is still unanswered and may be for some time.

As with SMGs, the number density of active galaxies appears to peak in the early universe around redshifts of 2-3. This is in line with the cosmic star formation rate density and shows a clear correlation between the two. Furthermore, there appears to be cosmic downsizing in AGN activity where the peak activity of more luminous AGN coincides with higher redshifts than that of their lower luminosity counterparts. For example, in a study of 508 active galaxies, La Franca et al. (2005) found that peak AGN activity for galaxies with $L_X \sim 10^{43}$ ergs s^{-1} was $z \sim 0.7$, while galaxies brighter than $L_X \sim 10^{45}$ ergs s^{-1} peaked at $z \sim 2.0$. This again falls in line with the cosmic star formation rate density and the downsizing of galaxies as a whole (Cowie et al. 1996). This poses problems for the widely accepted, bottom-up model of hierarchical structure formation, whereby small systems are created before large ones.

1.3.1 A Unified Model

Although observationally we see a variety of AGN, this has been explained by suggesting different viewing angles of a similar object. Dubbed the Unified Model, the idea is that all AGNs have the same basic structure with an accretion disk, dusty torus, broad line region, narrow line region etc. However, by observing these objects at different angles, we see different types of emission. Figure 1.1 shows an illustration of what the central engine of an AGN likely looks like. From the image it is easy to see why a unified model explains the differences we observe. By considering a viewing angle which would give clear access into the accretion disk, we would see a Seyfert I, as the broad and narrow line regions are unobstructed. Likewise, viewing the central engine through the dusty torus, the central core and broad line line region would be blocked, allowing only narrow line emission to be observed. Similarly, radio loud objects are viewed through a radio jet, while radio quiet objects are not.

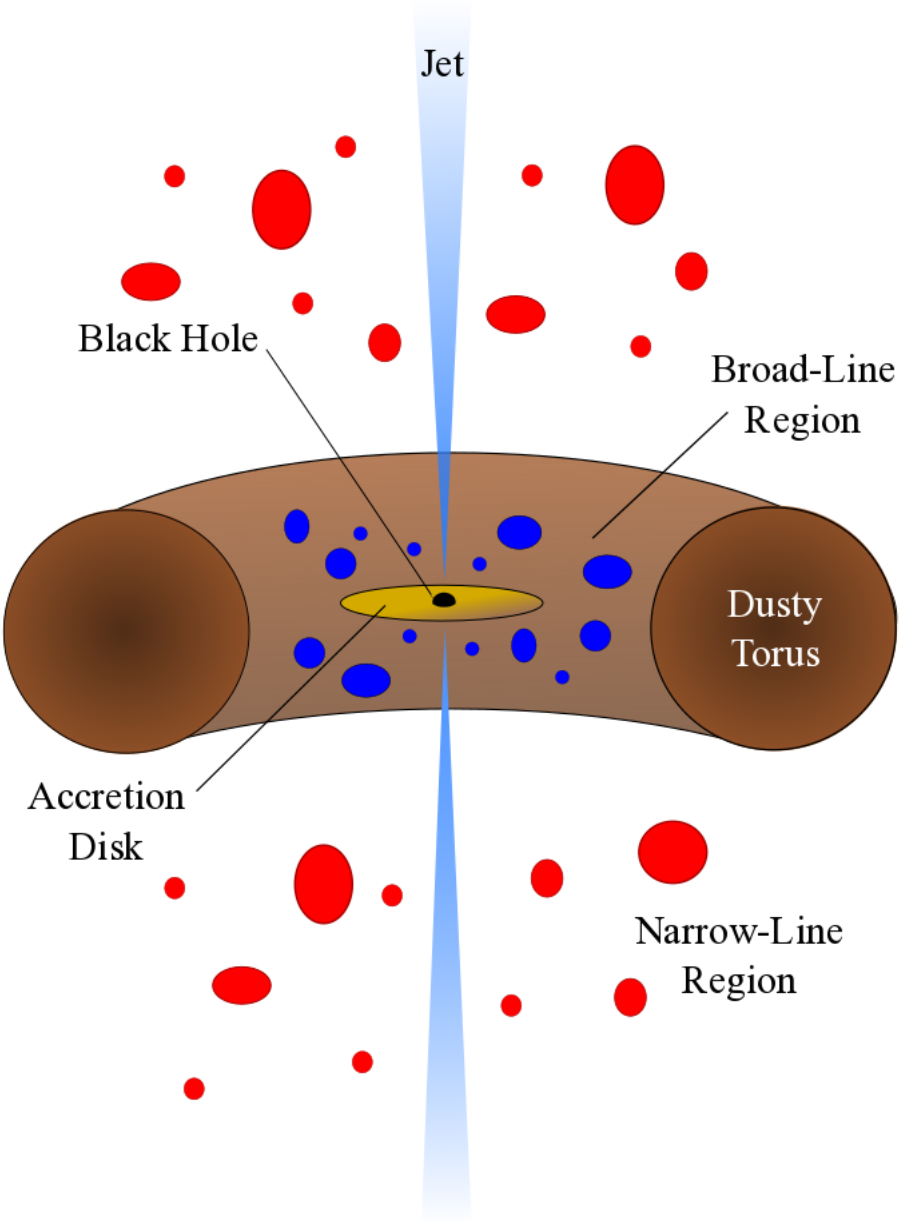

Figure 1.1: An illustration of the AGN Unified Model showing the accretion disk, black hole, dusty torus and both broad and narrow-line regions.

While the Unified Model works in most cases, and explains the differences between Seyfert I and Seyfert II galaxies (and viewing angles in between), it is not a perfect fit in all cases. For example, Bianchi et al. (2008) investigated NGC 3147 and showed that X-ray emission is unobscured and therefore should have both narrow and broad line emission. However, no broad line emission was observed which they attributed to the lack of a broad line region altogether. This object is one which they call a true Seyfert II, meaning that the broad line region is truly missing and not an inclination effect. Similarly, Brightman & Nandras (2008) found that both NGC 3147 and NGC 3660 may lack a broad line region altogether. Gallo et al. (2013) also found that AGN 1ES 1927+654 demonstrated optical properties of a Seyfert II, but showed little obscuration at X-ray wavelengths and rapid variability indicative of a direct view of the corona. While the majority of AGN discrepancies can be explained by different viewing angles of similar objects, it is now clear that not all cases fit this model exactly.

1.3.1.1 Dusty Torus

One of the key components in the unified model is the dusty torus. Composed of warm, molecular gas and dust, and thought to be in a toroidal distribution around the central engine, the dusty torus is responsible for the heightened infrared emission seen in most AGN. Although as yet unresolved[1], the torus plays both a physical and observational role in AGN. Physically, the torus helps to fuel the central engine. While long thought to be a passive fuel source for accretion, Hopkins et al. (2012) argue that the torus plays a much more functional role in AGN and actively drives accretion. While recent research has called into question the simplicity of the traditional toroidal model, for the purpose of this paper, a 'donut' shaped distribution is sufficiently complex.

[1] there are some papers claiming to have resolved a dusty torus, although this is still contested

As we have seen, the idea of a torus is the main culprit for viewing angle differences in the unified model. Although thought to be only a few parsecs in diameter, it is the dusty torus that has the most obvious effect on viewing angles as the torus is optically thick and obscures the central engine if viewed edge on. This is why we see still see the narrow line region when the torus is aligned along our line of sight, but fail to see the broad line emission indicative of Seyfert I galaxies. The idea of the obscuring torus was furthered by Antonucci & Miller (1985) who observed polarized broad line emissions in the Seyfert II galaxy NGC 1068. This emission, they postulated, was scattered out of an obscured broad line region and into the line of sight by free electrons surrounding the accretion disk. This was key in the unification of AGN because it showed that, while not directly observable, a broad line region still exists in the central core.

The torus itself is heated by the accretion disc and emits strongly in the infrared, providing evidence of the embedded AGN even while obscuring the central engine. Because the inner edge is closer to the accretion disk, there is a strong gradient of temperatures across the torus with emission ranging from the near infrared at the narrower radii, to the mid infrared at larger radii. Indeed, most Seyfert galaxies contain infrared, thermal 'humps' in their spectra that coincide with the idea of reradiated emission of the inner engine by dust. It is likely that the dust and gas in the torus is not smoothly distributed but is instead composed of individual and potentially turbulent clouds (Krolik & Begelman, 1998).

Chapter 2

Instrumentation

2.1 James Clerk Maxwell Telescope

All of the 850μm data for this study was collected with the the SCUBA-2 instrument on the JCMT. Although now operated by the East Asian Observatory, at the time of our data acquisition the JCMT was operated by the Joint Astronomy Centre, which was a collaboration among the United Kingdom, Canada, and the Netherlands. The JCMT is located on the summit of Mauna Kea on Big Island in Hawai'i were it has been operating since 1987.

Consisting of a 15 metre primary reflector, the JCMT is the largest submillimetre telescope in the world. The antenna is made of 276 aluminum coated panels who's alignment can be adjusted to a maintain surface accuracy of $\sim 24\mu$m. Covering the reflector is a large membrane of Gore-Tex (the largest in the world) which is 97% transparent at both millimetre and submillimetre wavelengths. The importance of the membrane is twofold: it is primarily to protect the antenna from wind, dust and the elements, but it also reflects both visible and near-infrared light, allowing for daytime and solar imaging.

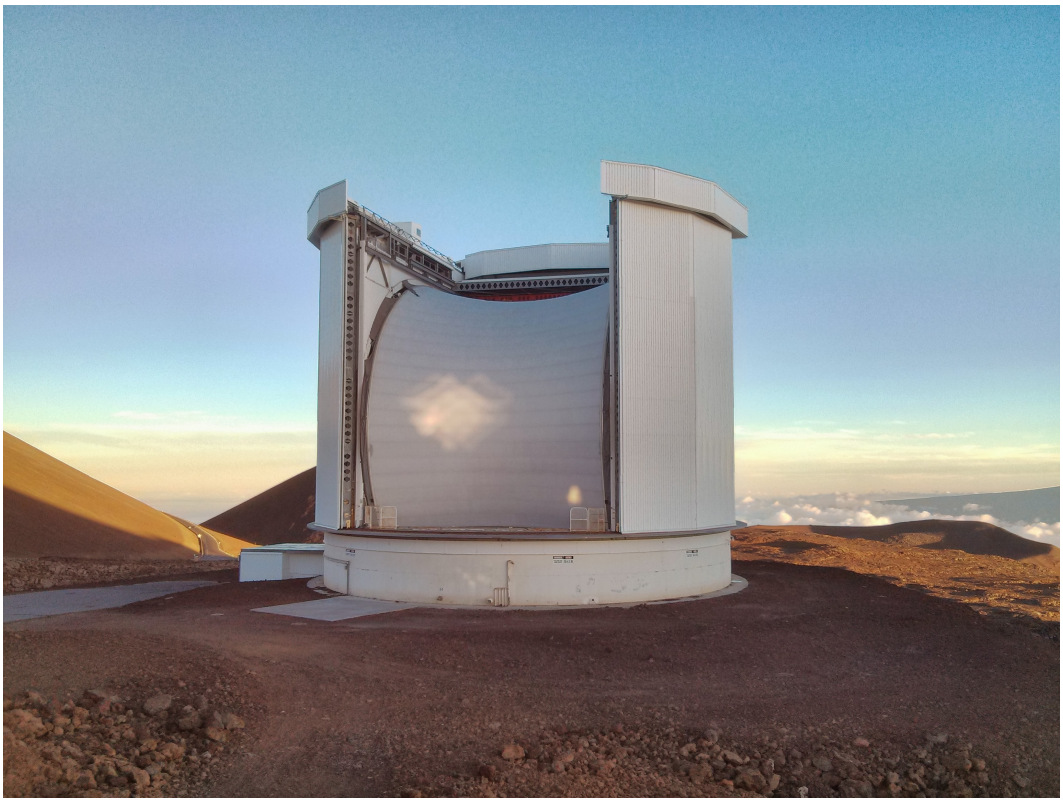

Figure 2.1: The JCMT observing in the evening.

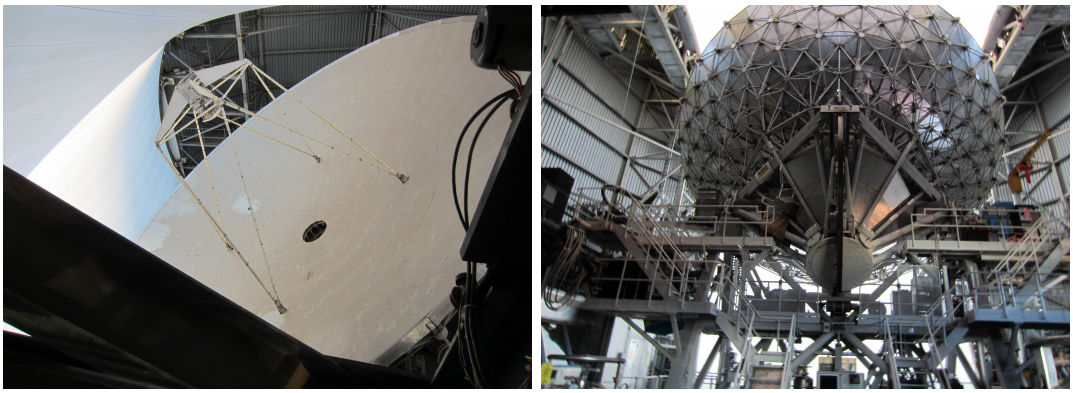

Figure 2.2: The 15 metre dish on the JCMT as seen from the front (left) and back (right).

2.1.1 SCUBA-2

The original broadband continuum receiver on the JCMT was the SCUBA instrument, which was in operation from 1997 to 2005. SCUBA operated at both 450μm and 850μm, with beam sizes of 15 arcseconds, and 7 arcseconds respectively. The original, blank field pointing preformed with the SCUBA instrument at 850μm was integral in the discovery of high redshift dusty galaxies. However, consisting of only 37 bolometers, mapping any reasonably sized area of sky was slow. This lead to the eventual commissioning of the SCUBA-2 instrument, which is in operation today.

In 2011, the 10,000 pixel bolometer camera, SCUBA-2, replaced the now retired SCUBA instrument. Like SCUBA, SCUBA-2 operates at both 450μm and 850μm but it utilizes large arrays of superconducting TESs, and has a mapping speed 100$-$150 times faster than that of its predecessor. The detector consists of two focal planes for observing at each wavelength, with 5,120 pixels in each plane, giving a total field of view of 45 arcminutes^2. Each focal plane is further broken down into four sub-arrays of 1,280 TES bolometers (Holland et al. 2013) made of molybdenum and copper. These bolometers have a transition temperature of 180 mK and 140 mK for 450μm and 850μm respectively, and couple directly to incident radiation.

SCUBA-2 utilizes two different mapping techniques. The first is the Constant Velocity (CV) Daisy which can map areas of up to 12 arcminutes^2 (although it was designed for small objects). The deep daisy is attained by observing in a roughly circular pattern around a set coordinate. The other method of mapping is with a Rotating Pong pattern, which is designed for mapping large areas. With this method, the telescope has a defined area to observe, and the beam 'reflects'

off the edge of the region to continue mapping. The CV Daisy produces a significantly deeper, but slightly smaller map than the Rotating Pong, making it a better choice for faint objects and fields.

Figure 2.3: The SCUBA-2 instrument (in blue) operating on the JCMT.

2.1.2 Work at JCMT

In order to better understand the JCMT, and submillimetre astronomy in general, I spent one week at JCMT working as the resident scientist. This consisted of nightly observing between 6pm and 6am, and included monitoring the queue and weather, and deciding which projects to observe. Because water vapour levels can change quite quickly on Mauna Kea, most of my time was spent monitoring these levels in order to switch between projects with better or worse weather condition criteria.

2.2 *Spitzer Space Telescope*

The 24μm data for this project was collected with the Multiband Imaging Photometer for *Spitzer* (MIPS) detector on the *Spitzer Space Telescope* (formerly the *Space Infrared Telescope Facility*). This infrared, space based telescope was launched in 2003 and was the final mission in NASA's Great Observatories Program. Although most space based telescopes have a geocentric orbit, *Spitzer* is rather unique in that it's orbit is heliocentric, trailing behind the Earth in its orbit at the L5 Lagrange point.

Spitzer is comprised of two main parts. The first is the Cryogenic Telescope Assembly which consists of an 85 centimetre telescope and three separate detectors: the Infrared Array Camera (IRAC), (MIPS), and the Infrared Spectrograph. The dish is a type of Cassegrain telescope called a Ritchey-Chrètien telescope, and is made entirely of beryllium. The second part of the observatory is the spacecraft, which both powers and controls the telescope, and communicates with earth. These two sections require two very different temperatures to operate. The electronics in the spacecraft need to run at room temperature, so this area is heated in order to maintain an optimal equipment temperature. The detectors and mirror, however, are cooled to 5.5K which is achieved using a tank of liquid helium.

Spitzer, like all space based telescopes, has a finite operational time span. This is because the onboard tank of cryogenic helium is limited and cannot be replaced. The original operation time span proposed for *Spitzer* was 2.5 years, however the coolant did not expire until 2009, nearly nearly 4 years longer than expected. The telescope now operates in what is known as the 'warm phase', and while most of the instruments no longer work, two channels on the IRAC instrument are still operational.

2.2.1 MIPS

While no longer operational, the MIPS instrument was a continuum camera which operated in the far-infrared. MIPS operated at 24μm, 70μm, and 160μm with beamsizes of 6 arcseconds, 17 arcseconds and 38 arcseconds respectively. It could also preform low resolution spectroscopy between 52μm and 100μm. While all of the wavebands imaged by MIPS were important, the 24μm channel was the most sensitive, and therefore, most widely used.

MIPS had three separate detectors for each waveband. The detector for 24μm imaging was comprised of one array of 16,384 arsenic-doped, silicon impurity band conduction (IBC) detectors which was cooled to $\sim$ 5.15K during operation (Rieke et al. 2004). The 52μm - 100μm and 160μm band detectors were made of 1,024 and 40, gallium-doped, germanium photoconductor arrays respectively. At 24μm, the field of view of the instrument was 25 arcminutes^2, and at 160μm it was only 2.5 arcminutes^2.

Chapter 3

Observations and Data Reduction

3.1 SCUBA-2 Imaging

3.1.1 850μm and 24μm Observations

The galaxies in our study reside in three fields (Q2343, Q1700 and Q1623), all three of which were imaged with the SCUBA-2 instrument on the JCMT, and the MIPS instrument on the *Spitzer Space Telescope*. The 24μm data is public access from the NASA/IRPAC Infrared Science Archive and was collected between April of 2005 and August of 2006. The 850μm observation details for each field are summarized in Table 3.1, and include the root mean square (RMS) noise level of the central region for both the 850 and 24μm data. All SCUBA-2 maps were acquired using the Deep Daisy mapping technique outlined in Section 2.1.1, and have a 15 arcsecond FWHM beam size.

3.1.2 Data Reduction

The deep, SCUBA-2 maps in this study were observed over several nights, resulting in separate data for each observation. Each night's observations consisted of a pre-observation flat field, the science scans, and a post-observation flat

Table 3.1: Observation Log

Field	Integration time (hours)	τ (CSO - 225 GHz)	Number of sources	σ_{850} (mJy)	σ_{24} (mJy)
Q2343	6	0.60	6	0.83	0.03
Q1700	15	0.50	6	0.5	0.04
Q1623	3	0.76	5	1.0	0.05

field. While the final flat field is not used, the first flat field and the science scans are reduced into a final night's map. Each night is reduced separately, and then combined. The data is reduced using the Dynamic Iterative Map Maker in the Sub-Millimeter User Reduction Facility (SMURF) package, which models each component of the bolometer signal, and iteratively removes them from the data. These steps are detailed in The SCUBA-2 Data Reduction Cookbook [64], as well as by Chapin et al. (2013), and are summarized here.

The first step in data reduction is the initial cleaning. To do this, the flat field is removed from the time series output from each seperate sub-array on the instrument. This is followed by a set of cleaning processes that apply non-iterative processes and glitch fixes which flag the worst data. First, the data is down-sampled, which is done by averaging several samples from the time-series to save time and memory. Steps in the time series (created by cosmic ray events) are sometimes seen in the data, so the next step involves their detection and removal. Any bad data (e.g. latching bolometers) which was removed is interpolated, and the iterative process can begin.

The iterative process attempts to model the signal recorded by the bolometers as a combination of several components. It then solves for the model by iterating until either a tolerance is reached, or a set number of iterations have been completed. The model components (as discussed by Chapin et al. 2013) can be seen in Table 3.2. Once the tolerance is reached, the cleaned time series for each bolometer is re-dispersed onto a map, and weighted according to time-domain variance. Finally, each night's reduced map is combined with the Pipeline for Combining and Analyzing Reduced Data (PICARD), which is included in the Starlink software package. The three combined fields can be seen in Figures 3.1 - 3.3.

Table 3.2: Model components of the SCUBA-2 signal.

Model Component	Description
COM	Models the common signal from all bolometers. This includes atmospheric noise, as well as any thermal instrument emission.
GAI	Models the gain and offset of each bolometer.
EXT	Corrects for extinction by applying a scaling factor based on current water vapour levels.
FLT	A Fourier Transform of the bolometer data which acts as a high or low-pass filter to remove noise.
AST	A map estimation for both signal and variance
NOI	A model of the RMS noise of each bolometer

3.1.3 Data

Table 3.3 summarizes the observations, as well as the CO-derived redshift of the Tacconi et al. (2013) sources. Cutouts of the fields with each object circled can be seen in Figures 3.1 - 3.3, and cutouts of each object at 850μm can be seen in Figure 3.4.

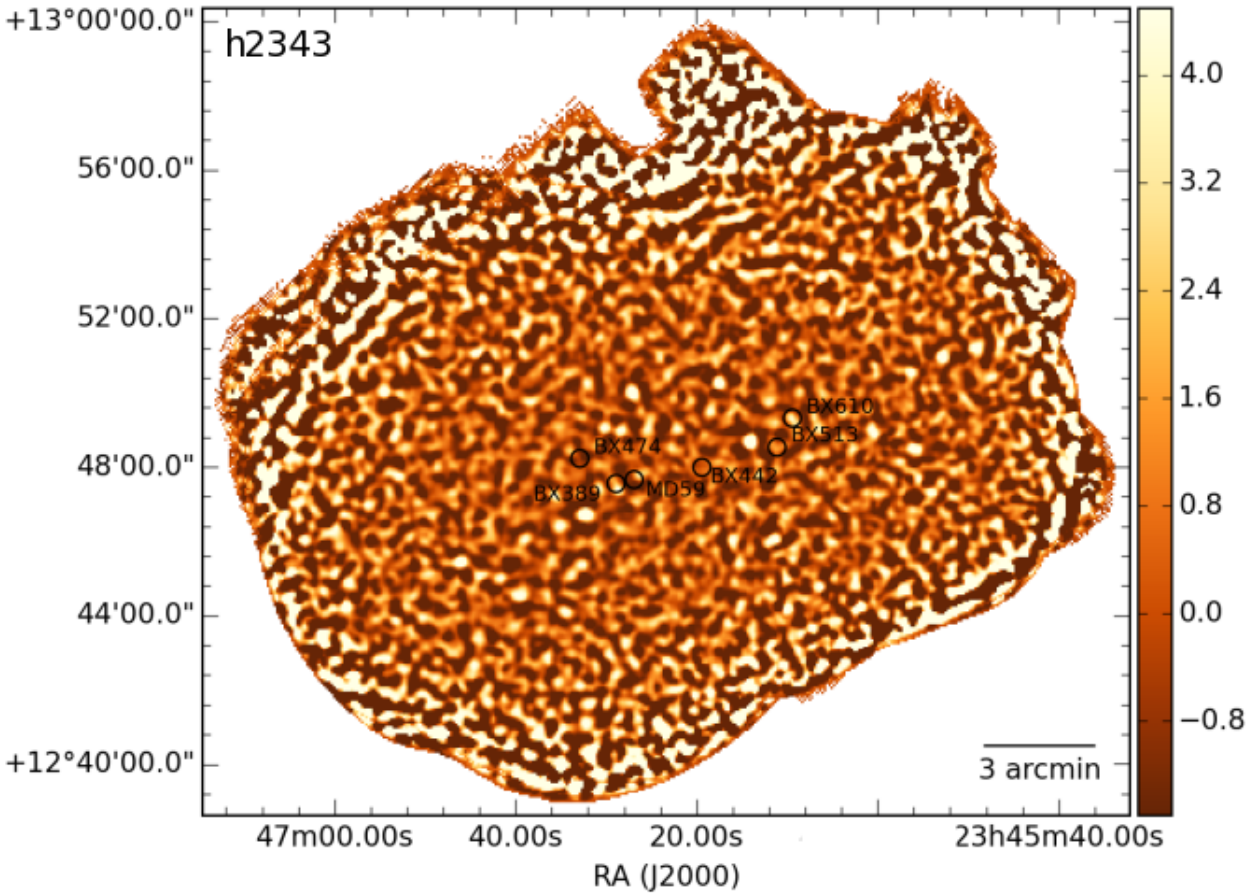

Figure 3.1: The Q2343 field with each object circled

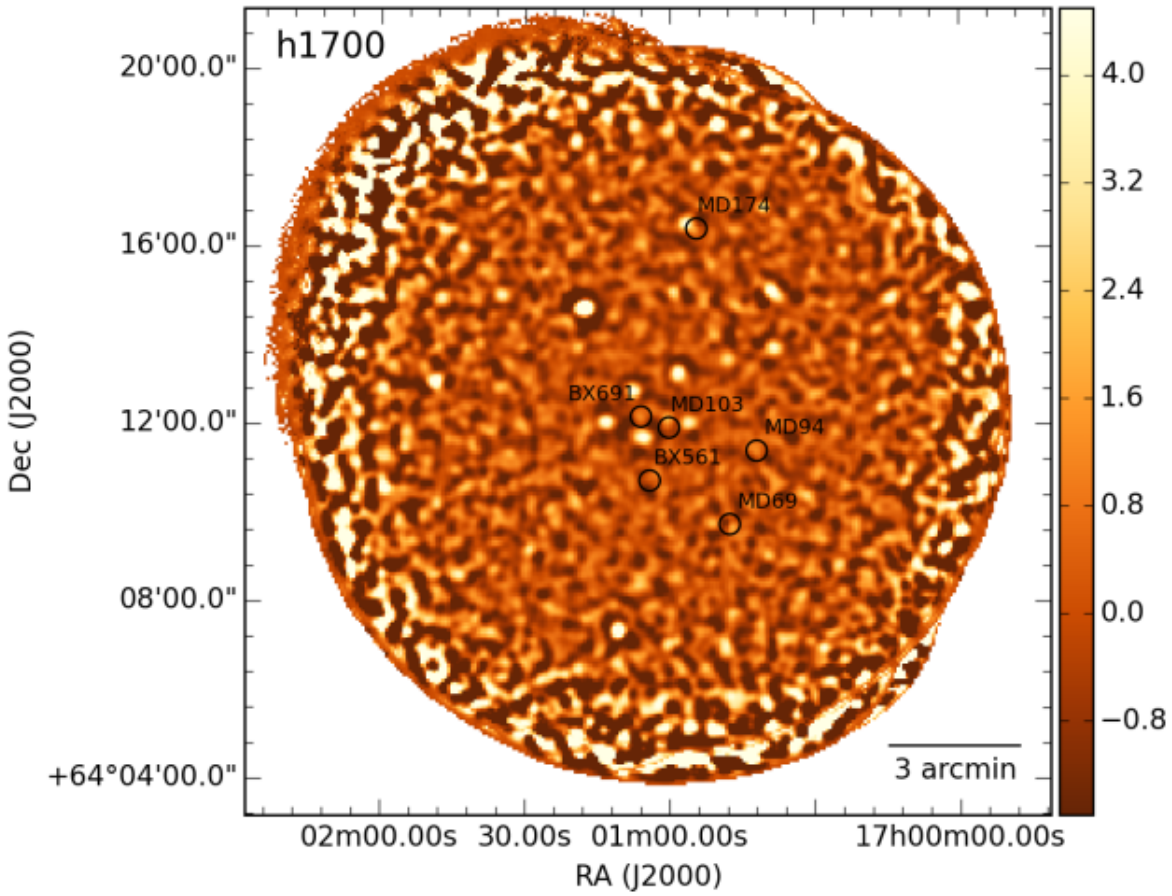

Figure 3.2: The Q1700 field with each object circled

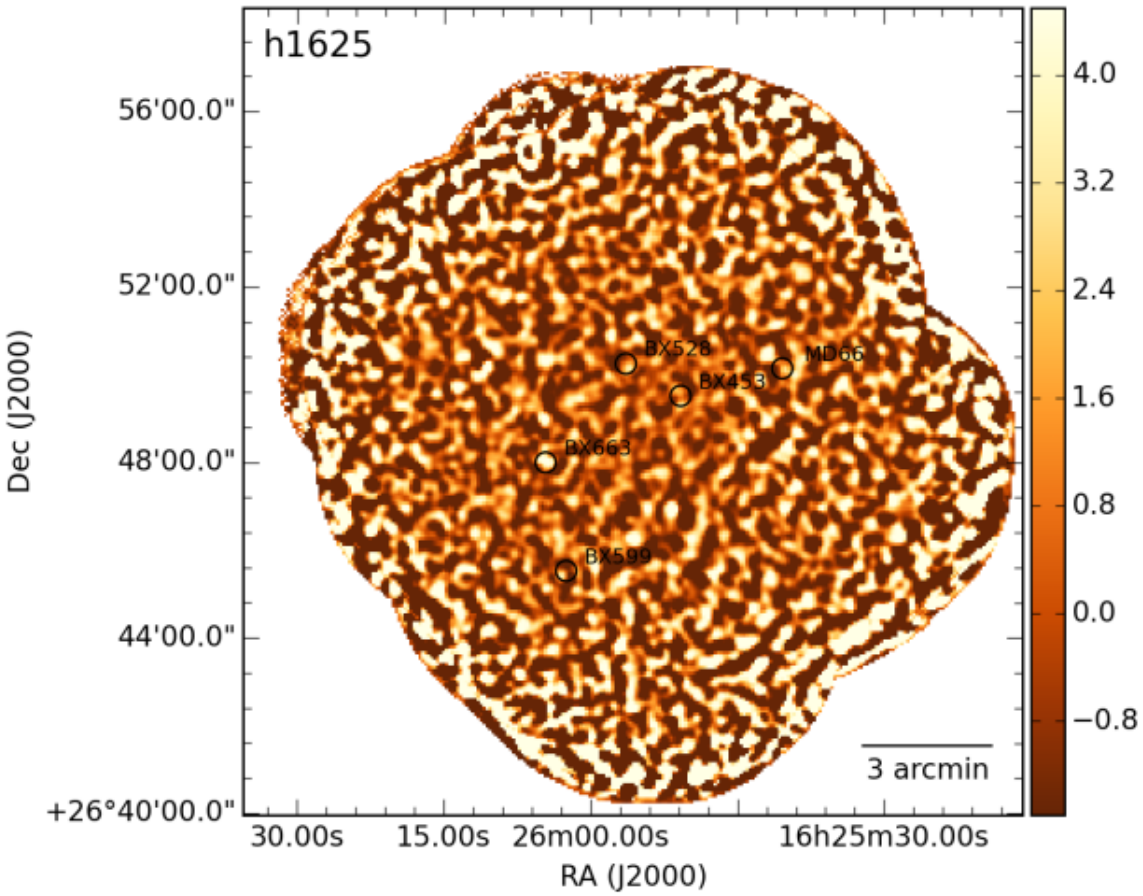

Figure 3.3: The Q1625 field with each object circled

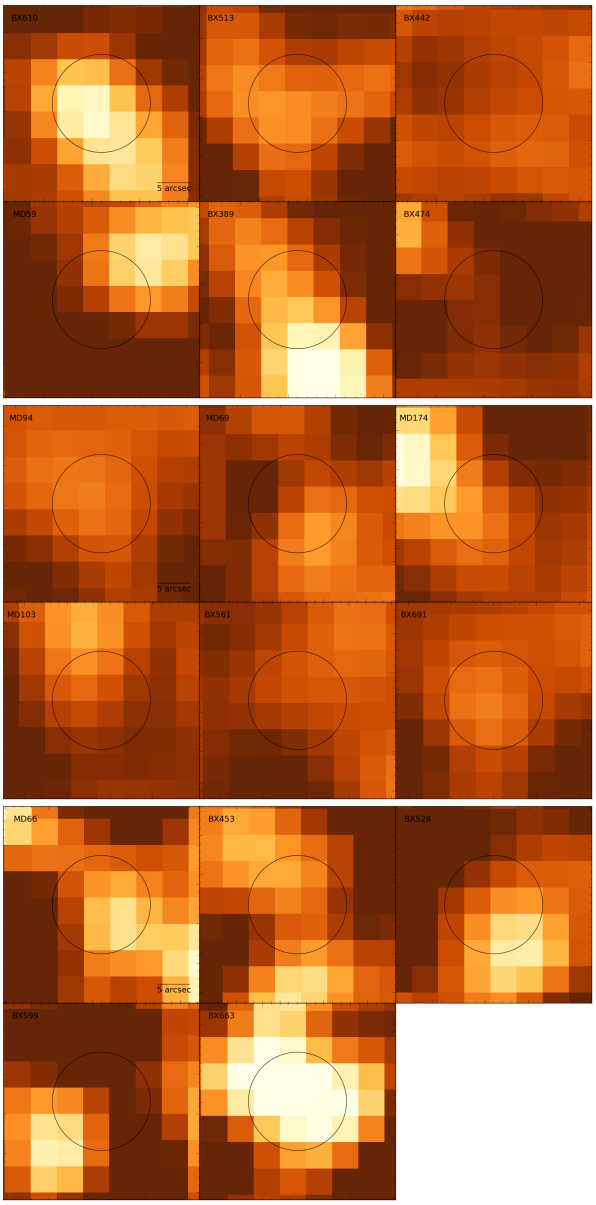

Figure 3.4: Cutouts of each object at 850μm. From top to bottom: Q2343, Q1700, and Q1625. The circle in each cutout represents the 15 arcsecond beam size of SCUBA-2.

Table 3.3: CO, 850μm and 24μm Observations

Source	α Optical	δ Optical	α CO	δ CO	$z_{\rm CO}$	S_{850} (mJy)	S_{24} (mJy)
Q2343−BX610	$23^{\rm d}46^{\rm h}09^{\rm s}.4$	$12^{\rm d}49'19''.2$	$23^{\rm d}46^{\rm h}09^{\rm s}.4$	$12^{\rm d}49'19''.3$	2.211	4.05±0.83	0.43±0.03
Q2343−BX513	$23^{\rm d}46^{\rm h}11^{\rm s}.1$	$12^{\rm d}48'32''.1$	$23^{\rm d}46^{\rm h}11^{\rm s}.1$	$12^{\rm d}48'31''.7$	2.1409	1.70±0.83	0.21±0.03
Q2343−BX442	$23^{\rm d}46^{\rm h}19^{\rm s}.4$	$12^{\rm d}47'59''.7$	$23^{\rm d}46^{\rm h}19^{\rm s}.3$	$12^{\rm d}47'58''.8$	2.175	2.49[a]	0.12±0.03
Q2343−MD59	$23^{\rm d}46^{\rm h}26^{\rm s}.9$	$12^{\rm d}47'39''.9$	$23^{\rm d}46^{\rm h}26^{\rm s}.9$	$12^{\rm d}47'39''.9$	2.011	2.49[a]	0.03±0.03
Q2343−BX389	$23^{\rm d}46^{\rm h}28^{\rm s}.9$	$12^{\rm d}47'33''.6$	-	-	-	2.49[a]	0.22±0.03
Q2343−BX474	$23^{\rm d}46^{\rm h}32^{\rm s}.9$	$12^{\rm d}48'14''.1$	-	-	-	2.49[a]	0.04±0.03
Q1700−BX691	$17^{\rm d}01^{\rm h}06^{\rm s}.0$	$64^{\rm d}12'10''.3$	$17^{\rm d}01^{\rm h}06^{\rm s}.1$	$64^{\rm d}12'10''.9$	2.189	1.31±0.5	0.24±0.04
Q1700−MD103	$17^{\rm d}01^{\rm h}00^{\rm s}.2$	$64^{\rm d}11'55''.5$	-	-	-	1.50[a]	0.29±0.04
Q1700−BX561	$17^{\rm d}01^{\rm h}04^{\rm s}.2$	$64^{\rm d}10'43''.8$	$17^{\rm d}01^{\rm h}04^{\rm s}.4$	$64^{\rm d}10'43''.8$	2.454	1.50[a]	0.28±0.04
Q1700−MD94	$17^{\rm d}00^{\rm h}42^{\rm s}.0$	$64^{\rm d}11'24''.2$	$17^{\rm d}00^{\rm h}42^{\rm s}.1$	$64^{\rm d}11'24''.0$	2.333	1.27±0.5	0.76±0.04
Q1700−MD69	$17^{\rm d}00^{\rm h}47^{\rm s}.6$	$64^{\rm d}09'44''.8$	$17^{\rm d}00^{\rm h}47^{\rm s}.6$	$64^{\rm d}09'44''.4$	2.289	1.80±0.5	0.23±0.04
Q1700−MD174	$17^{\rm d}00^{\rm h}54^{\rm s}.5$	$64^{\rm d}16'24''.8$	$17^{\rm d}00^{\rm h}54^{\rm s}.3$	$64^{\rm d}16'23''.3$	2.340	1.70±0.5	0.95±0.04
Q1623−MD66	$16^{\rm d}25^{\rm h}40^{\rm s}.4$	$26^{\rm d}50'08''.9$	-	-	-	5[a]	-
Q1623−BX456	$16^{\rm d}25^{\rm h}50^{\rm s}.8$	$26^{\rm d}49'31''.4$	$16^{\rm d}25^{\rm h}50^{\rm s}.9$	$26^{\rm d}49'31''.1$	2.182	3[a]	0.13±0.05
Q1623−BX528	$16^{\rm d}25^{\rm h}56^{\rm s}.4$	$26^{\rm d}50'15''.4$	$16^{\rm d}25^{\rm h}56^{\rm s}.6$	$26^{\rm d}50'13''.8$	2.268	3[a]	0.25±0.04
Q1623−BX599	$16^{\rm d}26^{\rm h}02^{\rm s}.5$	$26^{\rm d}45'31''.9$	$16^{\rm d}26^{\rm h}02^{\rm s}.6$	$26^{\rm d}45'31''.2$	2.330	3[a]	0.15±0.04
Q1623−BX663	$16^{\rm d}26^{\rm h}04^{\rm s}.6$	$26^{\rm d}48'00''.2$	$16^{\rm d}26^{\rm h}04^{\rm s}.6$	$26^{\rm d}47'59''.9$	-	5.59±1	0.64±0.04

[a] 3σ upper limit on sources.

3.2 Blending and a Multi-Wavelength Approach

One of the major problems with single dish submillimetre telescopes is the issue of multiplicity, which arises as a result of the large beam size of these telescopes. With upwards of 35% of single dish-detected SMGs being resolved into multiple component detections, this could be a significant problem for our study. To account for this, each source was studied at multiple wavelengths. Along with the 850μm and 24μm observations, 4.5μm IRAC images of the fields were used to determine if the submillimetre emission was coming from a single source or was blended. Multi-wavelength cutouts can be found in Figure 3.5, where the optical source coordinates are circled.

Some sources, such as BX610, had very well defined, single sources at 850μm, 24μm and 4.5μm. Some sources, however, seem to show submillimetre emission coming from multiple components; such is the case with MD103. Here, a very bright nearby source is seen at both 24 and 4.5 μm and is clearly dominating the emission. To eliminate bright sources and multiple detections, a bright, point-like source in the map was scaled to fit the peak flux of the source not in our sample. It was then subtracted from the map at the 4.5μm location, leaving only the submillimetre flux emitted by MD103. This was done for any 24μm sources that may have been blended (such as MD103) and the noise was re-measured.

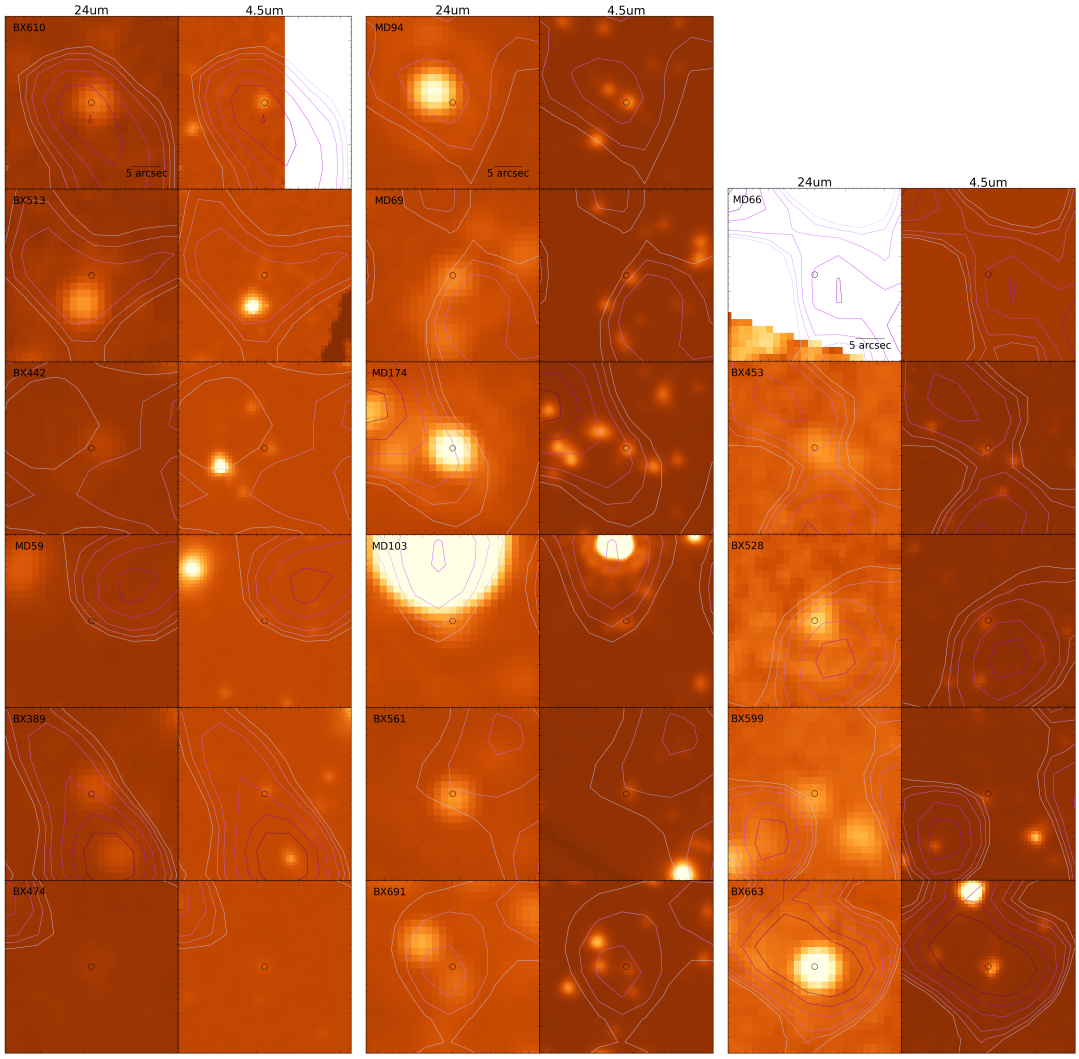

Figure 3.5: Cutouts of each object at both 24μm and 4.5μm. From left to right: Q2343, Q1700 and Q1625. Contours from the 850μm flux are included for each object as is the optical detection.

3.2.1 Jackknife Test

Because the detected 850μm emission of many of our sources is near the 3σ noise level, a psudo-jackknife test was used ensure that the measured fluxes were accurate (Staguhn et al. 2014). To do this, the reduced maps from each

night of observation were studied in detail. The idea is to look at each night's map before they are combined to make sure there are no noise spikes that dominate the final map. If the objects are detected in each night's map, we can be reasonably certain that it is a detection and not a large and random noise fluctuation. This test ensures that the detections we see (especially around the noise limit) are true and not an artifact of the instrument.

3.3 Stacking Analysis

The method of stacking multiple objects to boost the signal of faintly detected sources is one which was particularly useful to this study. Although only recently applied to submillimetre sources (Decarli et al. 2014), the method involves weighting multiple non-detections based on their specific noise (from the daisy noise profile), and then combining them. Of the 17 sources in our study, 10 of them were below the 3σ noise level, and were not well detected. All of these sources were considered 3σ upper limits and treated as such in the analysis. However, to further investigate these non-detections, a stacking analysis was done for each.

The stacking analysis was performed by first extracting a 25 arcsecond^2 region around (and including) the source. Each source was then weighted by the noise in the region around the object, and combined such that:

$$\langle S \rangle = \frac{\sum_j \frac{S_j}{\sigma_j^2}}{\sum_j \frac{1}{\sigma_j^2}} \tag{3.1}$$

where S is the signal of the individual object and σ is the RMS noise. The combined noise of the stacked detections is:

$$\sigma^2 = \frac{\sum_j \sigma_j}{\sqrt{N}} \tag{3.2}$$

where N is the total number of objects in the stack. The result of the stacking analysis was a well defined source at at 0.9 ± 0.2 mJy.

Chapter 4

Results

4.1 Molecular Gas Mass

Interstellar, molecular gas in a galaxy is extremely important to our understanding of galaxy evolution. This is because this cold gas tends to congregate in large, dense clouds which eventually collapse into new stars. In fact, star formation is confined exclusively to these clouds, and so the amount of gas available in a galaxy can give us an idea of how much fuel the galaxy has remaining.

The majority of interstellar, molecular gas in galaxies is in the form of molecular hydrogen (H_2), however, H_2 is notoriously hard to observe directly. This is because H_2 has no permanent, electric dipole moment, and therefor does not radiate. It is still possible to measure molecular gas mass however, by observing molecules known to 'trace' molecular hydrogen. One of these molecules is carbon monoxide (CO) which is not polar symmetric, and so it couples with an incident photon and radiates at it's rotational frequency (projected normal to the line of sight). We can therefore infer gas masses from this molecule, even though it is both significantly less common than molecular hydrogen and is optically thick.

The gas masses reported here were derived by Tacconi et al. (2013) who used the line flux from the CO (3-2) transition to derive the molecular gas mass for all of the PHIBSS galaxies (a method originally applied by Solomon et al. 1997). Following along with Tacconi et al. (2013), the gas mass was derived by:

$$M_{gas}/M_{\odot} = 1.75 \times 10^{9} \left(\frac{\alpha}{\alpha_G}\right) \left(\frac{F_{\mathrm{CO}J}}{\mathrm{Jy\,km\,s^{-1}}}\right) \times (R_{J1})\,(1+z)^{-3} \left(\frac{\lambda_{\mathrm{obs}J}}{\mathrm{mm}}\right)^{2} \left(\frac{D_L}{\mathrm{Gpc}}\right)^{2} \tag{4.1}$$

where α and α_G are the conversion factors from CO to H_2 (for the star forming population, and the Milky Way respectively), $F_{\mathrm{CO}\,J}$ is the CO line flux for the J $\rightarrow$ J$-$1 transition, z is the redshift of the object, and D_L is the luminosity distance. The value R_{J1} is included out of a need to convert from CO 3$-$2 transition to the CO 1$-$0 transition. Tacconi et al. (2013) use a conversion factor of:

$$R_{J1} = R_{13} = \frac{L'_{\mathrm{CO}\,1-0}}{L'_{\mathrm{CO}\,3-2}} \sim 2 \tag{4.2}$$

where L'_{CO} is the line luminosity, given by the integrated Rayleigh-Jeans source brightness Temperature (T_{RJ}) as a function of Doppler velocity (υ):

$$L'_{\mathrm{CO}} = T_{RJ}\, d\upsilon\, dA. \tag{4.3}$$

The conversion factor, α, between $\mathrm{M_{CO}}$ and $\mathrm{M_{mol\text{-}gas}}$ depends on the type of galaxy being observed, and is an average over a specific population. This conversion factor is defined by:

$$\alpha_{\mathrm{CO}\,J} = h \left(\frac{(\langle n\,(\mathrm{H_2})\rangle)^{1/2}}{T_{RJ}}\right) g\,(Z) \tag{4.4}$$

where $\langle n\,(\mathrm{H_2})\rangle$ is the average gas cloud density, T_{RJ} is the is the Rayleigh-Jeans brightness temperature of a specific CO conversion, and $g(Z)$ is metallicity. Tacconi et al. (2013) took the galactic factor, α_G, to be 4.36 $\pm$ 0.9 $\mathrm{M_{\odot}/(K\ km\ s^{-1}\ pc^{-2})}$, which is true for local, low metallicity galaxies, as well as the Milky Way (e.g. Bolatto et al. 2013). They argue that this is also a good estimate for

the PHIBSS galaxies because the CO emission in the high redshift, star-forming galaxies arises in virialized giant molecular clouds, similar to that of the local galaxies we see today. The gas masses derived by Tacconi et al. (2013) are outlined in Table 4.1, and include a 36% mass correction for helium.

4.2 Star Formation Rates

4.2.1 Submillimetre Derived Star Formation Rates

While the best way to accurately describe the SFR of a galaxy is by incorporating a large range of observations at multiple wavelengths, it is possible (although not necessarily accurate) to derive a SFR given a specific wavelength. While Tacconi et al. (2013) used optical and UV emission to derive star formation rates, an independent method of defining a galaxy's SFR is by using the 850μm flux.

The $S_{850}-$SFR relation is derived from the infrared luminosity-to-SFR relation described by Kennicutt et al. (1998), given by:

$$\frac{\mathrm{SFR}}{1\ M_{\odot}\,\mathrm{yr}^{-1}} = \frac{L_{\mathrm{IR}}}{2.2\times10^{43}\,\mathrm{ergs\,s}^{-1}} = \frac{L_{\mathrm{IR}}}{5.8\times10^{9}\ L_{\odot}}. \tag{4.5}$$

The negative k-correction for submillimetre wavelengths means that this relation is straightforward at high redshift. Because the flux does not change with redshifts higher than ~ 1.5, this luminosity relation can be converted directly into a flux relation, suitable for nearly all star forming galaxies above $z \sim 1.5$. Although generally derived using the spectral fitting of Arp 220 over the $8-100\mu$m range, Barger at al. (2014), found that the relation:

$$SFR_{850} = 200 \times S_{850} \tag{4.6}$$

is a better fit their sample of galaxies, rather than the Arp 220 derived relation of:

$$SFR_{850} = 180 \times S_{850}. \tag{4.7}$$

Therefore, it is the Barger et al. (2014) relation that we have adopted here.

A summary of the resulting 850μm star formation rates can be found in Table 4.1. The derived star formation rates are plotted in Figure 4.1, where they are compared to both the optical/UV derived SFR, as well as that of 24μm.

4.2.2 24μm Derived Star Formation Rates

A third method of determining star formation rates is by using 24μm emission. At redshifts $\sim$ 2 (as are the galaxies in our sample), the observed frame 24μm emission is dominated by vibrational emission from PAHs, which are a good indicator of the B-type stars which dominate galactic luminosity (Peeters, Spoon & Tielens, 2004). PAHs are primarily excited by UV photons which are produced in abundance by massive, B-type stars, who's relatively short lifespans are indicative of ongoing star formation. PAH emission is also especially good at boosting the emission signal at the observed frame 24μm (which would traditionally be faint at high redshifts due to cosmological dimming), therefore making the observation easier.

Although not as straightforward as the 850μm SFR derivation, deriving a 24μm SFR is possible. The idea is to use the 24μm emission to extrapolate a total infrared luminosity ($L_{TIR} = L_{(8-1000\mu\mathrm{m})}$) by using SED templates. This was done by Chary & Elbaz et al. (2001) and Elbaz et al. (2002), who produced templates for a variety of rest frame calibrations. The one most useful here is:

$$L_{\mathrm{IR}} = 4.78^{+2.37}_{-1.59} \times (\nu L_{\nu}[6.75\,\mu\mathrm{m}])^{0.998} \tag{4.8}$$

Table 4.1: Derived properties of the sample galaxies.

Source	F(CO) (Jy km s^{-1})	SFR$^{a}_{H\alpha+UV}$ (M$_\odot$ yr^{-1})	SFR$_{850}$ (M$_\odot$ yr^{-1})	SFR$_{24}$ (M$_\odot$ yr^{-1})	M$_{mol-gas}$^{b} ($10^1$0 M$_\odot$)	M$_{dust}$ (10^9 M$_\odot$)
Q2343−BX610	0.95±0.05	212	811 ± 166	118 ± 70	23	3.1 ± 0.6
Q2343−BX513	0.15±0.05	28	340 ± 166	51 ± 40	3.2	1.3 ± 0.6
Q2343−BX442	0.27±0.07	145	498^{c}	32 ± 17	6.2	1.9^{c}
Q2343−MD59	0.47±0.09	26	498^{c}	7 ± 5	9.5	1.9^{c}
Q2343−BX389	0.51^{c}	196	498^{c}	69 ± 45	1.2^{c}	1.9^{c}
Q2343−BX474	0.29^{c}	62	498^{c}	13 ± 10	7.0^{c}	1.9^{c}
Q1700−BX691	0.18±0.05	50	263 ± 100	39 ± 30	4.1	1.0± 0.4
Q1700−MD103	0.41^{c}	104	300^{c}	86 ± 60	1.1^{c}	1.2^{c}
Q1700−BX561	0.12±0.04	17	300^{c}	96 ± 62	3.410	1.2^{c}
Q1700−MD94	1.24±0.20	271	254 ± 100	238 ± 148	33	0.98± 0.4
Q1700−MD69	0.38±0.06	164	359 ± 100	69 ± 47	9.6	1.4± 0.4
Q1700−MD174	0.64±0.08	159	331 ± 100	299 ± 190	17	1.3± 0.4
Q1623−MD66	0.5^{c}	246	600^{c}	-	1.1^{c}	2.3^{c}
Q1623−BX453	0.38±0.05	246	600^{c}	34 ± 27	8.9	2.3^{c}
Q1623−BX528	0.19^{c}	59	600^{c}	74 ± 49	4.8^{c}	2.3^{c}
Q1623−BX599	0.19±0.04	131	600^{c}	46 ± 39	5.0	2.3^{c}
Q1623−BX663	0.28 ^{c}	144	1118 ± 200	191 ± 117	7.9^{c}	4.3± 0.8

^{a} ±35% systematic uncertanty

^{b} ±50% systematic uncertanty

^{c} 3σ upper limit

for $\nu L_\nu(6.75\,\mu\mathrm{m}) \leq 5 \times 10^9 L_\odot$, and:

$$L_{\mathrm{IR}} = 4.37^{+2.35}_{-2.13} \times 10^{-6}(\nu L_\nu[6.75\,\mu\mathrm{m}]) \tag{4.9}$$

for $\nu L_\nu(6.75\,\mu\mathrm{m}) \geq 5 \times 10^9 L_\odot$ (Caputi et al. 2006). The luminosities for both equations are in solar units.

These equations are useful to our sample because rest frame 24μm emission between $2 \leq z \leq 3$ is approximately 6.75μm, and so this template was adopted to convert our fluxes to total infrared luminosity. To calculate the SFR, Equation 4.5 was used with the derived infrared luminosity. The 24μm derived SFRs can be seen in Table 4.1, and the comparison to that of the UV/optical and 850μm derived rates are shown in Figure 4.1.

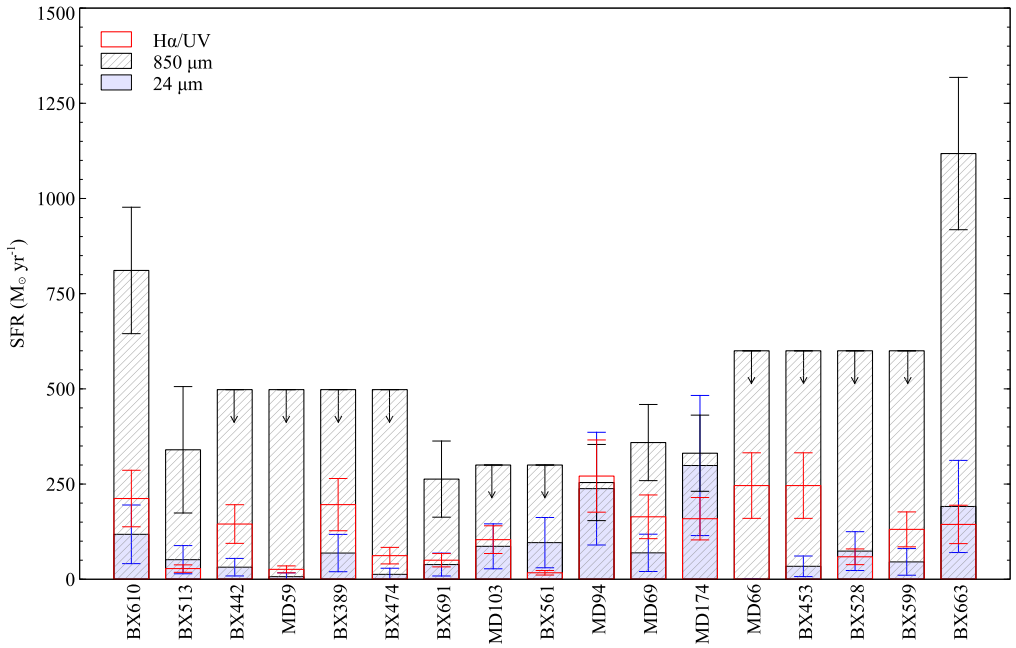

Figure 4.1: Star formation rates derived both by the Hα and UV emission (Tacconi et al. 2013) shown in red, 850μm flux (black), and 24μm flux (blue). Although most agree to within uncertainty, the SFR of both BX610 and BX663 are significantly underestimated by the Hα and UV emission.

4.3 Dust Mass

Emission at 850μm is dominated by cool dust, making the submillimetre waveband ideal for calculating dust mass. This has traditionally been derived using the following equation (e.g. Dunne, Eales & Edmonds 2003):

$$M_{dust} = \frac{S_{850} \times D_L}{\kappa_\nu \times B_\nu(T)} \tag{4.10}$$

where D_L is the luminosity distance, κ_ν is the dust mass absorption coefficient, and $B_\nu(T)$ is the value of the Planck function at temperature, T. Genzel et al. (2015), however, found that an alternate estimate could be obtained using the derived SFR. Using dust as a calorimeter, which is optically thin and radiating at an average temperature, they found that the dust mass can be derived using:

$$M_{\rm dust} = 1.2 \times 10^{15}\,({\rm SFR}) \times T_{\rm dust}^{-5.5} \tag{4.11}$$

where $T_{\rm dust}$ is the modified blackbody dust temperature, taken here to be 35K. The SFR is in $M_\odot$ yr^{-1} and the dust mass is in $M_\odot$. It is this equation that we adopted to calculate dust mass, and we used the 850μm derived SFR because it most represents the modified blackbody 'hump' of dust emission.

The derived dust masses of the galaxies in our sample can be seen in Table 4.1. Figure 4.2 shows the calculated gas-to-dust ratio as a function of both the 850μm and 24μm derived SFRs.

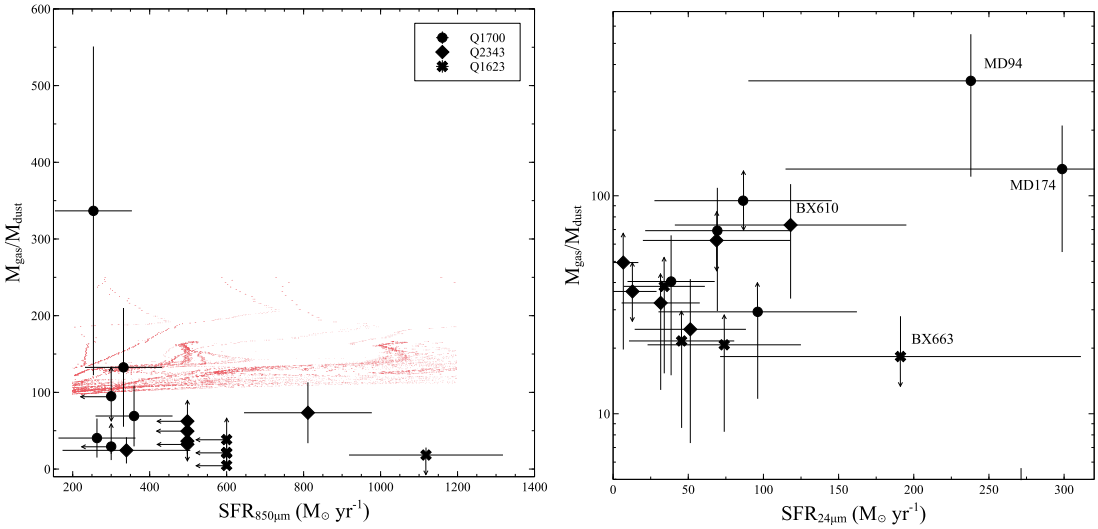

Figure 4.2: The ratio of molecular gas mass to the 850 μm derived dust mass. (Left) The 850 μm derived SFR is plotted here with tracks from the simulation by Hayward et al. (2011) (red), which used major mergers to produce M_{gas} and S_{850} properties. It is important to note that the simulation data in the upper left corner is highly dependent on the initial conditions of the simulation, and should be interpreted as such. (Right) The same gas-to-dust ratio is plotted here except with the independently derived 24μm SFR. Note the two Q1700 outliers which are possible AGN

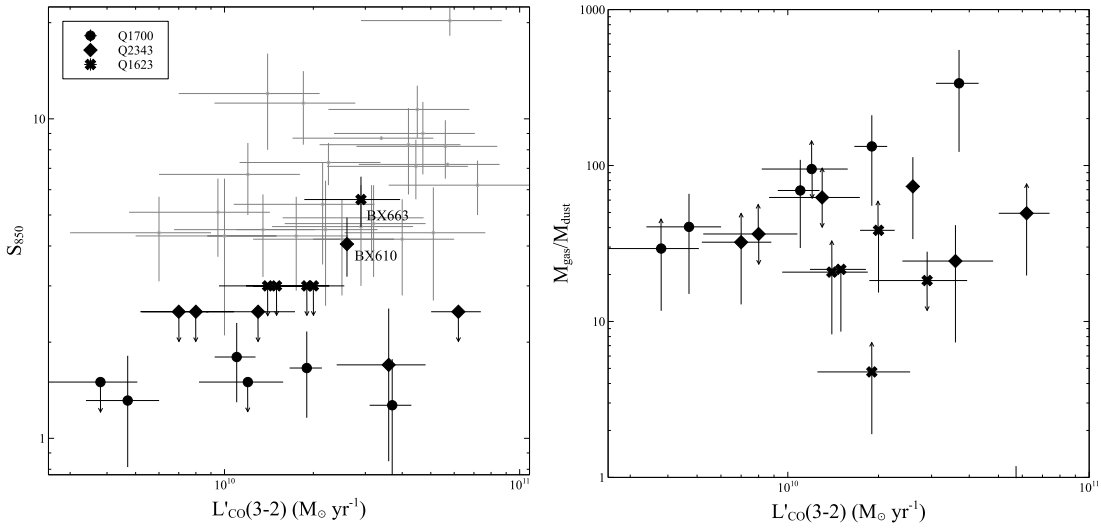

Figure 4.3: (Left) The 850μm flux plotted against the CO (3-2) line luminosity highlights the two submillimetre bright sources. The gray data points are taken from Bothwell et al (2013) and are a sample of SMGs at $z \approx 2$. While the majority of the galaxies in this sample are where we would expect, the two bright 850μm sources fit nicely with the SMGs. (Right) The ratio of the CO derived gas mass to the submillimetre derived dust mass.

Chapter 5

Discussion

5.1 BX610

BX610 is one of the most well defined galaxies in our sample. It is sub-millimetre bright, and has a high enough flux to be considered an SMG. This is highlighted in the left panel of Figure 4.3, which shows the 850μm flux as a function of CO line luminosity. The gray points in the upper right corner are submillimetre sources (at redshifts comparable to ones in this study), taken from Bothwell et al. (2013), and BX610 resides within these objects. This means that, although considered to be a regular, star forming galaxy in the PHIBSS survey, it is in fact something different and needs to be treated as such.

As a follow up to the 850 and 24μm analysis, we analyzed the near-infrared spectra of BX610. Figure 5.1 shows the two dimensional spectra for the galaxy with wavelength along the bottom and position across the galaxy as the width. The bright, central emission line is that of Hα, and the [NII] doublet can be seen on either side. This shows clearly that this is a star forming galaxy and that there is no obvious AGN to widen the Hα line.

What is interesting about this source is that is has a very high CO derived gas mass, which offsets its high 850μm derived dust mass when looking at the gas-to-dust ratio. Indeed, with the exception of MD94, BX610 has the highest gas mass of all the high redshift PHIBSS objects. The fact that this galaxy is an SMG, however, may explain this. The derivation by Tacconi et al. (2013) assumed

that all of the galaxies were regular star-formers, and therefore used a conversion factor of $\alpha_{CO} = 4.36$ in their calculations. This is not accurate for SMGs, and a value of $\alpha_{CO} \sim 0.8$ (Solomon et al. 1997, Downes & Solomon 1998, Tacconi et al 2008) is more appropriate, which decreases the derived gas mass of this galaxy by a factor of five. The corrected gas mass was found to be $4.2 \times 10^{10} M_{\odot}$, and can be seen in Figure 5.6.

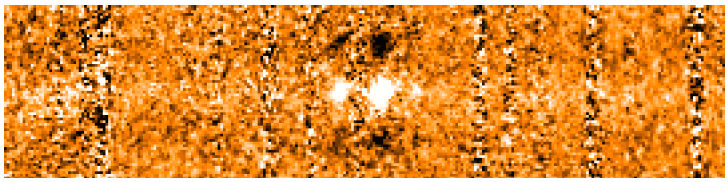

Figure 5.1: The two dimensional spectra of BX610. The strong central line is that of Hα and the [NII] doublet can be seen on either side.

5.2 BX663

The other bright submillimetre source in our sample is BX663. The noise in the Q1625 map is quite high compared to the other maps, but while all other Q1625 sources are upper limits, BX663 is a 3σ detection. With a brighter flux than BX610, this galaxy can be also be considered an SMG, and has similar consequences.

While the 850μm flux (and therefore the dust mass) is well detected, the CO emission is an upper limit and so the gas mass is unconstrained. Even unconstrained, the upper limit on the gas mass will decrease by a factor of five as a result of the more accurate derivation with $\alpha_{CO} = 0.8$. The corrected upper limit of $1.4 \times 10^{10} M_{\odot}$ can be seen in Figure 5.6

As with BX610, follow up was done with near infrared spectra. A strong, central Hα line as well as an [NII] doublet was seen in this galaxy as well, and is shown in Figure 5.2. Again, this shows that no obvious AGN is present and that our initial SMG classification is correct.

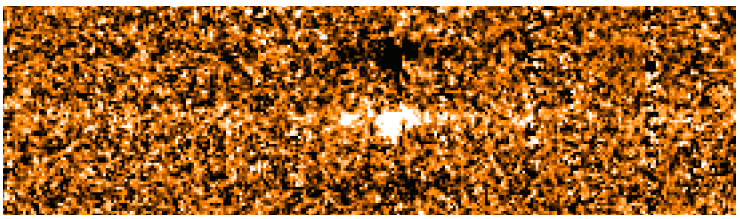

Figure 5.2: The two dimensional spectra of BX663. As with BX610, the strong central line is that of Hα and the [NII] doublet can be seen on either side.

5.3 MD174

The brightest 24μm source in our sample is MD174. Given that it has such a high 24μm flux, we conclude that this galaxy likely hosts an AGN. As previously discussed, 24μm emission at these redshifts has two possible sources, either from starburst activity or a dusty torus surrounding the central engine of an AGN. Both the 850μm and the optical/UV derived SFRs for this galaxy are not particularly high, and so starburst processes do not easily describe the 24μm emission seen here. This is highlighted in Figure 5.5 where a colour-magnitude diagram shows this galaxy and one other as outliers in the top left corner. We therefore conclude that the emission is driven by the torus surrounding an embedded AGN, and so the galaxy as does not behave like its more passive counterparts. This means that, as with the two SMGs in the sample, this galaxy is not a regular, star forming galaxy and should not be treated as such. It also means that the 24μm derived

SFR is not reliable because the emission is not star-formation driven, and so it should not be given any weight.

Figure 5.3 shows the NIR spectra of MD174. The emission line seen in the figure is from Hα but it has been widened significantly which we attribute to the presence of an AGN. Although the emission line is not widened significantly enough to imply broad line region velocities, the suggested velocities are considerably higher than those found in the disk of a regular star forming galaxy. It is likely that the broadening of the line is coming from high velocity gas around the AGN, and so the Hα/UV derived SFR from Tacconi et al. (2013) is questionable. Similar to SMG, AGN gas mass should be derived with an α_{CO} factor of 0.8, and the corrected gas mass for MD174 was found to be $3.1 \times 10^{10} M_{\odot}$.

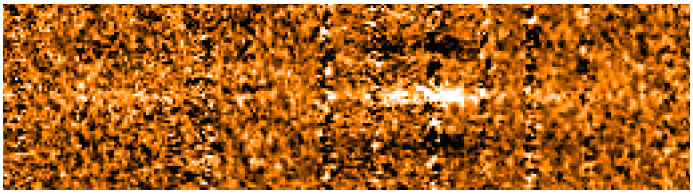

Figure 5.3: The two dimensional spectra of MD174. The line in the middle is Hα but it has been significantly widened due to the presence of an AGN.

5.4 MD94

MD94 is also a very bright 24μm source, which we likewise conclude to be an AGN. Although dimmer than MD174, it is still considerably brighter at 24μm than it is at 850μm and Figure 5.5 clearly shows it is an outlier as the second source in the top left corner.

Similar to MD174, Figure 5.4 shows the NIR spectra of MD94. As with the other AGN, the central Hα line is significantly broadened and so we are confident

in our initial conclusions that MD94 hosts an AGN. This means that the 24μm derived SFR should not be given any weight because the emission is likely from the dusty torus. The Hα/UV derived SFR should be questioned as well. This source has the highest CO derived gas mass within the high redshift sample, which we now believe to be incorrect. As with the other AGN and SMGs, the gas mass was recalculated with $\alpha_{CO} = 0.8$ and was found to be $6.1 \times 10^{10} M_{\odot}$, lowering it by a factor of five. This brings it in line with the gas mass of the other high redshift galaxies, and the corrected gas-to-dust ratio plots can be seen in figure 5.6.

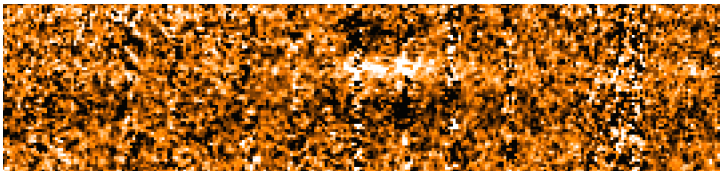

Figure 5.4: The two dimensional spectra of MD94. As with MD174, the central emission line is Hα and it has been widened by the central AGN.

5.5 Star Formation

Each method of deriving SFR assumes something about the galaxy in question, and each has their own strengths and weaknesses. Figure 4.1 shows all three derived star formation rates for the galaxies in the study, and there are some obvious discrepancies. Most obvious are BX610 and BX663, which have 850μm derived star formation rates that are significantly higher than both the 24μm and Hα/UV. While this may be a dust temperature effect (see Section 5.7.1), it questions the Tacconi et al. (2013) estimates. Likewise, while the 850μm emission from BX561 is an upper limit, the 24μm derived star formation rate is much higher than that of the Hα/UV, which is quite small. While most of the

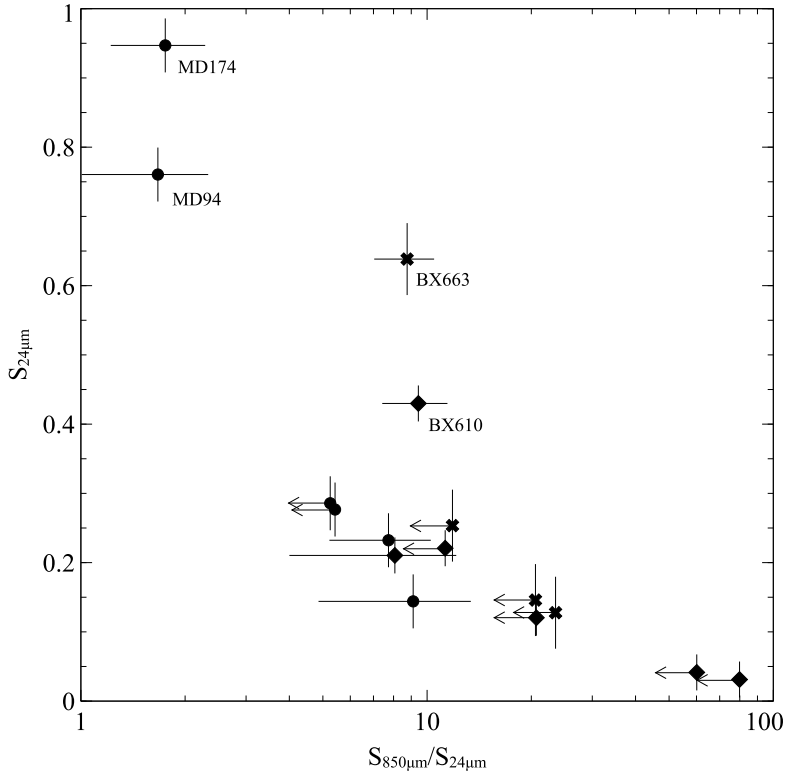

Figure 5.5: This colour-magnitude diagram highlights both MD174 and MD94 as anomalies in the top left corner. The high 24μm flux and relatively average 850μm emission points to the idea that these two sources are likely AGNs. While BX610 and BX663 also emit strongly at 24μm, their spectra shows no Hα broadening so they likely do not host an AGN.

star formation rates are in reasonable agreement, these outliers do pose a valid question about the accuracy of single wavelength SFR derivations.

The 850μm derived SFR becomes particularly important when dealing with the two active galaxies in our sample. As previously stated, the 24μm emission from these two galaxies cannot be used as an appropriate representation of star formation, and the Hα emission is questionable as well. This means that the most accurate estimation of SFR is from the submillimetre, which, while still affected by the AGN, is the best indicator presented here. This has implications for figures in this paper. Figure 4.2 (and corrected for gas mass in Figure 5.6) shows the gas-to-dust ratio vs. both the 24μm and 850μm derived SFR. While the 850μm derived SFR plot is degenerate (both the dust mass and SFR are 850μm derived), in some ways it is more accurate than its non-degenerate counterpart because of the two AGN. This is also seen in Figure 5.6, where the gas mass is corrected, but the 24μm derived SFR is still shown for these two galaxies.

5.6 Gas and Dust

The gas-to-dust ratios for each object can be seen in Figure 4.2 and Figure 4.3, and corrected in Figure 5.6. While the gas-to-dust vs. 850μm derived SFR is degenerate at 850μm, and should be treated as such, the gas-to-dust vs. 24μm and gas-to-dust vs. L'$_{3\text{-}2}$(CO) plots are interesting. Both plots appear to show a possible trend towards increased gas-to-dust ratios for increased CO line luminosity and SFR. However, this trend changes dramatically when the gas mass estimates are corrected. Figure 5.6 shows the corrected ratios for these same three plots. While the gas-to-dust vs. 850μm plot is still degenerate (hence the distribution), the other two plots have changed. The apparent trend towards higher gas-to-dust ratios for higher CO line luminosity and SFR disappears when

a more accurate measure of gas mass is applied, and both plots appear to show a relatively constant gas-to-dust ratio.

The effect that the corrected gas mass made on these plots is important for two reasons. While obviously important for the change in gas-to-dust ratio, it says something about the importance of contamination in a sample of galaxies. Four, of seventeen objects with overestimated gas mass were enough to skew the sample, creating a non-existent correlation. This highlights the fact that a multi-wavelength, observational approach is imperative to both large and small scale studies of star forming galaxies.

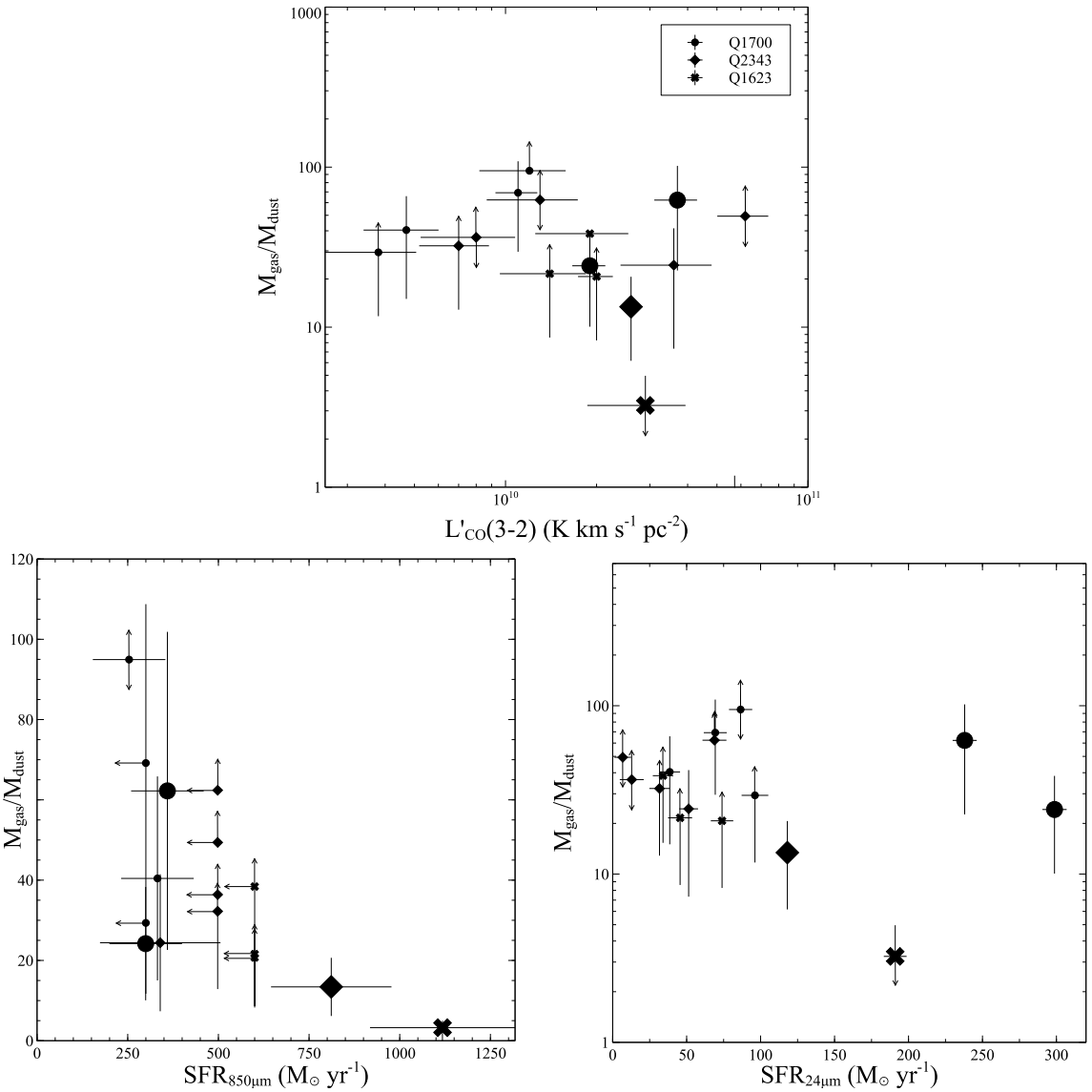

Figure 5.6: The three gas-to-dust plots corrected for gas mass. The corrected objects are shown as bolded points.

5.7 Degeneracies and Derivation Issues

5.7.1 Dust Temperature at 850μm

One major issue in determining the star formation rate from 850μm flux, is that the luminosity at wavelengths greater than 500μm is heavily impacted by dust temperature. At 850μm, the measured flux density at a given redshift (e.g. $z \sim 2$), change by a factor of 4 for two similar galaxies with T_{dust} = 30K and 50K. This greatly impacts the calculated SFR (and dust mass), as the basis for our derivation is directly related to the measured 850μm flux and luminosity (uncorrected for T_{dust}) (Blain et al. 2004). In fact, for galaxies with redshifts of $z \sim 2$ (as are the galaxies in our sample), the 850um flux follows the relation $S_{850} \simeq T_{dust}^{-3.5} L_{TIR}$. Not only does this impact SFR calculations, it also contributes to a selection bias known as the submillimetre dust temperature selection effect, whereby SMGs with dust temperatures greater than 50K fall below the noise threshold of many instruments at 850μm.

The dust temperature we assumed for all of the galaxies in the sample was 35K, which is a reasonable estimate. For example, Swinbank et al. (2013) found the dust temperature of 99 SMGs to be well constrained at 32 $\pm$ 1 K. Similarly, Magnelli et al. (2010) found the dust temperature to be 36 $\pm$ 8 K, but use a much smaller sample size. While our estimates of dust temperature are reasonable, it is important to note that a galaxy with a boosted dust temperature would appear to have a higher 850μm derived SFR and dust mass than reality.

5.7.2 Gas Mass From a Single CO Transition (J = 3-2)

Estimating gas mass is difficult because the bulk of the ISM is composed of molecular hydrogen. Molecular hydrogen is extremely important in the ISM because these cool gas clouds are the basis for star formation. The issue is that H_2 cannot be observed directly and so an indirect method of measurement is

necessary. As previously discussed, Tacconi et al. (2013) use CO (3-2) emission to probe the molecular gas mass of the galaxies in their sample.

While the conversion factor for CO to H_2 has been discussed (and corrected in four galaxies in the sample), it is important to discuss this factor in more detail. While it has been well studied in local galaxies, the conversion can vary greatly depending on metallicity and gas density. Both dusty star-formers and regular, star forming galaxies can vary drastically in morphology, and using a single ratio for a large group of diverse galaxies can be problematic. Furthermore, Magnelli et al. (2012) found that the conversion factor changes with dust temperature, which adds further ambiguity. The idea that the conversion factor is either 0.8 or 4.3 is also problematic because these factors are averaged over total populations, and so there is a good chance that many of our objects lie somewhere between these two values.

Another problem with CO derived gas mass is that the radiation from intense star forming regions can substantially change gas clouds. CO molecules are photodissociated more easily than the H_2 regions they trace, and so the CO in diffuse gas clouds may be broken down while the H_2 remains intact. This is important in intense star forming regions because the radiation will break down CO molecules before H_2. While this is not a problem in Milky Way type galaxies (Neininger et al. 1998), our sample of galaxies are actively star forming, which may be an issue if CO molecules are being destroyed. Furthermore, Papadopoulos et al. (2012) shows that in local ULIRGs, using low J-CO lines systematically underestimates gas mass because gas is so turbulent. However, they did find that well sampled, higher transitions (including J = 3-2, as was done in Tacconi et al. (2013)) are better at H_2 mass estimates.

Chapter 6

Conclusions

Of the seventeen galaxies in the high redshift PHIBSS sample at least 24% were not, in fact, regular, star forming galaxies. Two of the seventeen were found to be submillimetre galaxies, and two host obscured active galactic nuclei. It could be argued also that some of the objects with $S_{850} \sim 3$ could have lower conversion factors as well That is a considerable amount of contamination, and can easily skew the sample, as shown by the corrected gas-to-dust ratio plots in Figure 5.6. It is therefore important not to rely on the UV waveband alone in the selection of galaxies on the star forming 'main-sequence'. It is important to have multi-wavelength data, not only to derive accurate characteristics of these galaxies, but to make sure they are, in fact, what they are supposed to be.

While each of the derived star formation rates has issues, a single method approach has obvious shortcomings. Both the 24μm and 850μm derivations show underestimates in SFR, which, while potentially attributed to dust temperature, require further investigation. Without observing at submillimetre wavelengths, dusty star-formers will be overlooked. This is a serious issue because their intrinsically high SFRs can have disproportionately large impacts. Furthermore, the 850μm derived SFR is much more accurate for the two SMGs, who's UV and optical emission is diminished by dust absorption. This is also true of the two AGN because the dust continuum is not greatly impacted by the presence of a central engine.

Although the sample is small, when corrected gas masses are taken into consideration, there appears to be no clear relation between increased gas-to-dust

ratio and both SFR and CO line luminosity for actively star forming, high redshift galaxies. While there is considerable scatter, likely driven by the fact that these galaxies are not in the same stage of evolution, this conclusion makes sense. Both dust mass and gas mass independently scale with SFR (e.g. Santini et al. 2014), so it is a reasonable assumption that the gas-to-dust ratio will not change.

Bibliography

[1] Antonucci, R. R. J. & Miller, J.S. Spectropolarimetry and the nature of NGC 1068. *The Astrophysical Journal* **297**, 621-632 (1985)

[2] Barger, A. J. Cowie, L. L. & Wang, W. -H. The Microjansky Radio Galaxy Population. *The Astrophysical Journal* **654**, 764-781 (2007)

[3] Barger, A. J. et al. Is There a Maximum Star Formation Rate in High-redshift Galaxies? *The Astrophysical Journal* **784**, 9-31 (2014)

[4] Blain, A. W. et al. Submillimeter Galaxies. *Physics Reports* **369**, 111-176 (2002)

[5] Blain, A. W. Chapman, S. C., Smail, I. & Ivison, R. Accurate Spectral Energy Distributions and Selection Effects for High-Redshift Dusty Galaxies: A New Hot Population to Discover with the Spitzer Space Telescope? *The Astrophysical Journal* **611**, 52-58 (2004)

[6] Bianchi et al. NGC 3147: a 'true' type 2 Seyfert galaxy without the broad-line region. *Monthly Notices of the Royal Astronomical Society* **385**, 195-199 (2008)

[7] Bolatto et al. The CO-to-H_2 Conversion Factor. *Annual Review of Astronomy and Astrophysics* **51**, 207-268 (2013)

[8] Bothwell, M. S. et al. A survey of molecular gas in luminous sub-millimetre galaxies. *Monthly Notices of the Royal Astronomical Society* **429**, 3047-3067 (2013)

[9] Brightman & Nandras On the nature of unabsorbed Seyfert 2 galaxies. *Monthly Notices of the Royal Astronomical Society* **433**, 421-433 (2013)

[10] Casey, C. M. et al. Characterization of SCUBA-2 450 μm and 850 Îijm selected galaxies in the COSMOS field. *Monthly Notices of the Royal Astronomical Society* **436**, 1919-1954 (2013)

[11] Casey, C. M., Naratanan, D. & Cooray, A. Dusty star-forming galaxies at high redshift. *Physical Reports* **541**,45-161 (2014)

[12] Chapin, E. L. et al. SCUBA-2: iterative map-making with the Sub-Millimetre User Reduction Facility. *Monthly Notices of the Royal Astronomical Society* **430**, 2545-2573 (2013)

[13] Chapman, S. C., Blain, A. W., Ivison, R. J. & Smail, I. A median redshift of 2.4 for galaxies bright at submillimetre wavelengths. *Nature* **422**, 695-698 (2003)

[14] Chapman, S. C., Blain, A. W., Smail, I. & Ivison, R. J. A redshift survey of the submillimeter galaxy population. *The Astrophysical Journal* **622**, 772-796 (2005)

[15] Chary, R. & Elbaz, D. Interpreting the Cosmic Infrared Background: Constraints on the Evolution of the Dust-enshrouded Star Formation Rate. *The Astrophysical Journal* **556**, 562-581 (2001)

[16] Cowie, L. L. et al. New Insight on Galaxy Formation and Evolution From Keck Spectroscopy of the Hawaii Deep Fields. *Astronomical Journal* **112**, 839-864 (1996)

[17] Cuputi, K. I. et al. Linking Stellar Mass and Star Formation in Spitzer MIPS 24 μm Galaxies. *The Astrophysical Journal* **637**, 727-740 (2006)

[18] Decarli, R. et al. An ALMA Survey of Sub-millimeter Galaxies in the Extended Chandra Deep Field South: Sub-millimeter Properties of Color-selected Galaxies. *The Astrophysical Journal Letters* **780**, 115-127 (2014)

[19] Dopcke, G. et al. The Effect of Dust Cooling on Low-metallicity Star-forming Clouds. *The Astrophysical Journal Letters* **729**, 3-10 (2011)

[20] Downes, D. & Solomon, P. M. Rotating Nuclear Rings and Extreme Starbursts in Ultraluminous Galaxies. *The Astrophysical Journal* **507**, 615-654 (2018)

[21] Dunne, L., Eales, S. A. & Edmunds, A census of metals at high and low redshift and the connection between submillimetre sources and spheroid formation. *Monthly Notices of the Royal Astronomical Society* **341**, 589-598 (2003)

[22] Elbaz, D. et al. The bulk of the cosmic infrared background resolved by ISOCAM. *Astronomy & Astrophysics* **384**, 848-865 (2002)

[23] Ellison, S. L., Patton, D. R. & Hickox, R. C. Galaxy pairs in the Sloan Digital Sky Survey - XII. The fuelling mechanism of low-excitation radio-loud AGN. *Monthly Notices of the Royal Astronomical Society* **451**, 35-39 (2015)

[24] Erb, D. et al. Hα Observations of a Large Sample of Galaxies at $z \sim 2$: Implications for Star Formation in High-Redshift Galaxies. *The Astrophysical Journal* **647**, 128-139 (2006)

[25] Gallo, L. C. et al. 1ES 1927+654: a bare Seyfert 2. *Monthly Notices of the Royal Astronomical Society* **390**, 1241-1249 (2008)

[26] Gaskell, C. M., Goosmann, R. W. & Klimek, E. S. Structure and kinematics of the broad-line region and torus of Active Galactic Nuclei. *Memorie della Societa Astronomica Italiana* **79**, 1090-1095 (2008)

[27] Genzel, R. et al. Combined CO and Dust Scaling Relations of Depletion Time and Molecular Gas Fractions with Cosmic Time, Specific Star-formation Rate, and Stellar Mass. *The Astrophysical Journal* **800**, 20-45 (2015)

[28] Greve, T. R. et al. An interferometric co survey of luminous submillimetre galaxies. *Monthly Notices of the Royal Astronomical Society* **359**, 1165-1183 (2005)

[29] Hai, F. et al. The rapid assembly of an elliptical galaxy of 400 billion solar masses at a redshift of 2.3. *Nature* **498**, 338-341 (2013)

[30] Hayward, C. C. et al. What Does a Submillimeter Galaxy Selection Actually Select? The Dependence of Submillimeter Flux Density on Star Formation Rate and Dust Mass. *The Astrophysical Journal* **743**, 159-173 (2011)

[31] Hayward, C. C. et al. Spatially unassociated galaxies contribute significantly to the blended submillimetre galaxy population: predictions for follow-up observations of ALMA sources. *Monthly Notices of the Royal Astronomical Society* **434**, 2572-2581 (2013)

[32] Hodge, J. A. et al. An ALMA survey of submillimeter galaxies in the Extended Chandra Deep Field South: Source catalog and multiplicity. *The Astrophysical Journal* **768**, 91-111 (2013)

[33] Holland, W. S. et al. SCUBA-2: The 10000 pixel bolometer camera on the James Clerk Maxwell Telescope. *Monthly Notices of the Royal Astronomical Society* **430**, 2513-2533 (2013)

[34] Hopkins, P. et al. The origins of active galactic nuclei obscuration: the 'torus' a dynamical, unstable driver of accretion. *Monthly Notices of the Royal Astronomical Society* **420**, 320-339 (2012)

[35] Hughes, D., H. et al. High-redshift star formation in the Hubble Deep Field revealed by a submillimetre-wavelength survey. *Nature* **394**, 241-247 (1998)

[36] Ivison, R. J. et al. A hyperluminous galaxy at z=2.8 found in a deep sub-millimetre survey. *Monthly Notices of the Royal Astronomical Society* **298**, 583-593 (1998)

[37] Kennicutt, R. C. et al. The global Schmidt law in star forming galaxies. *The Astrophysical Journal* **498**, 541-552 (1998)

[38] Krolik, J. H. & Begelman, M. C. Molecular tori in Seyfert galaxies: Feeding the monster and hiding it. *The Astrophysical Journal* **329**, 702-711 (2013)

[39] La Franca, F. et al. The HELLAS2XMM Survey. VII. The Hard X-Ray Luminosity Function of AGNs up to z = 4: More Absorbed AGNs at Low Luminosities and High Redshifts. *The Astrophysical Journal* **635**, 864-879 (2005)

[40] Lagache, G. et al. Polycyclic Aromatic Hydrocarbon Contribution to the Infrared Output Energy of the Universe at $z \simeq 2$. *The Astrophysical Journal Supplement Series* **154**, 112-117 (2004)

[41] Magnelli, B., et al. Far-infrared properties of submillimeter and optically faint radio galaxies. *Astronomy & Astrophysics* **518**, 28-32 (2010)

[42] Magnelli, B., et al. Dust temperature and CO - H_2 conversion factor variations in the SFR-$M_\star$ plane. *Astronomy & Astrophysics* **548**, 22-37 (2012)

[43] Neininger, N., et al. Carbon monoxide emission as a precise tracer of molecular gas in the Andromeda galaxy. *Nature* **395**, 871-873 (1998)

[44] Papadopoulos, P. P. et al. The molecular gas in luminous infrared galaxies - I. CO lines, extreme physical conditions and their drivers. *Monthly Notices of the Royal Astronomical Society* **426**, 2601-2629 (2012)

[45] Papadopoulos, P. P. et al. The Molecular Gas in Luminous Infrared Galaxies. II. Extreme Physical Conditions and Their Effects on the X_{co} Factor. *The Astrophysical Journal* **751**, 10-39 (2012)

[46] Peeters, E., Spoon, H. W. W & Tielens, A. G. G. M. Polycyclic Aromatic Hydrocarbons as a Tracer of Star Formation? *Astronomy & Astrophysics* **613**, 986-1003 (2004)

[47] Riechers, D. A. et al. A Dust-Obscured Massive Maximum-Starburst Galaxy at a Redshift of 6.34. *Nature* **496**, 329-333 (2013)

[48] Rieke, G. H. et al. The Multiband Imaging Photometer for *Spitzer* (MIPS). *The Astrophysical Journal Supplement Series* **154**, 25-29 (2004)

[49] Rowlands, K. et al. Herschel-ATLAS: properties of dusty massive galaxies at low and high redshifts. *Monthly Notices of the Royal Astronomical Society* **441**, 1017-1039 (2014)

[50] Rowlands, K. et al. The dust budget crisis in high-redshift submillimetre galaxies. *Monthly Notices of the Royal Astronomical Society* **441**, 1040-1058 (2014)

[51] Santini, P. et al. The dust content of high-z submillimeter galaxies revealed by Herschel. *Astronomy and Astrophysics* **518**, 154-160 (2010)

[52] Santini, P. et al. The evolution of the dust and gas content in galaxies. *Astronomy and Astrophysics* **562**, 30-58 (2014)

[53] Scoville, N. et al. The Evolution of Interstellar Medium Mass Probed by Dust Emission: ALMA Observations at $z = 0.3$-2. *The Astrophysical Journal* **783**, 84-97 (2014)

[54] Simpson, J. M. et al. An ALMA Survey of Submillimeter Galaxies in the Extended Chandra Deep Field South: The Redshift Distribution and Evolution of Submillimeter Galaxies. *The Astrophysical Journal* **788**, 125-169 (2014)

[55] Smail, I., Ivison, R. J., Blain, A. W. & Kneib, J.-P. The nature of faint submillimetre-selected galaxies. *Monthly Notices of the Royal Astronomical Society* **331**, 495-520 (2002)

[56] Solomon, P. M. et al. The molecular interstellar medium in ultraluminous infrared galaxies. *The Astrophysical Journal* **478**, 144-161 (1997)

[57] Staguhn, J. G. et al. The GISMO Two-Millimeter Deep Field in GOODS-N. *The Astrophysical Journal* **790**, 77-93 (2014)

[58] Steidel, C. C. et al. A Survey of Star-forming Galaxies in the $1.4 \lesssim z \lesssim 2.5$ Redshift Desert: Overview. *The Astrophysical Journal* **640**, 534-550 (2004)

[59] Swinbank, A. M. et al. The link between submillimetre galaxies and luminous ellipticals: near-infrared IFU spectroscopy of submillimetre galaxies. *Monthly Notices of the Royal Astronomical Society* **371**, 465-476 (2006)

[60] Swinbank, A. M. et al. An ALMA Survey of Sub-millimetre Galaxies in the Extended Chandra Deep Field South: The Far-Infrared Properties of SMGs. *Monthly Notices of the Royal Astronomical Society* **438**, 1267-1287 (2014)

[61] Tacconi, L. J. et al. Submillimeter Galaxies at $z \sim 2$: Evidence for Major Mergers and Constraints on Lifetimes, IMF, and CO-H_2 Conversion Factor. *The Astrophysical Journal* **680**, 246-262 (2008)

[62] Tacconi, L. J. et al. High molecular gas fractions in normal massive star-forming galaxies in the young Universe. *Nature* **463**, 781-784 (2010)

[63] Tacconi, L. J. et al. Phibss: Molecular Gas Content and Scaling Relations in z 1-3 Massive, Main-sequence Star-forming Galaxies. *The Astrophysical Journal* **768**, 74-96 (2013)

[64] Thomas, H. S. & Currie, M. J. The SCUBA-2 Data Reduction Cookbook (v.1.3). Science and Technology Facilities Counsil (2014)

[65] Vieira, J. D. et al. Dusty starburst galaxies in the early Universe as revealed by gravitational lensing. *Nature* **495**, 344-347 (2013)